Article

SOURCE DATA | TRANSPARENT PROCESS | OPEN ACCESS

THE EMBO JOURNAL

The CUL4B-based E3 ubiquitin ligase regulates mitosis and brain development by recruiting phospho-specific DCAFs

Anna Stier[1,†], Samuel Gilberto[1,†,‡], Weaam I Mohamed[1,†], Lars N Royall[2], Jonne Helenius[3], Ivan Mikicic[4], Tatjana Sajic[5,§], Petra Beli[4,6], Daniel J Müller[3], Sebastian Jessberger[2] & Matthias Peter[1,*]

Abstract

The paralogs CUL4A and CUL4B assemble cullin-RING E3 ubiquitin ligase (CRL) complexes regulating multiple chromatin-associated cellular functions. Although they are structurally similar, we found that the unique N-terminal extension of CUL4B is heavily phosphorylated during mitosis, and the phosphorylation pattern is perturbed in the CUL4B-P50L mutation causing X-linked intellectual disability (XLID). Phenotypic characterization and mutational analysis revealed that CUL4B phosphorylation is required for efficient progression through mitosis, controlling spindle positioning and cortical tension. While CUL4B phosphorylation triggers chromatin exclusion, it promotes binding to actin regulators and to two previously unrecognized CUL4B-specific substrate receptors (DCAFs), LIS1 and WDR1. Indeed, co-immunoprecipitation experiments and biochemical analysis revealed that LIS1 and WDR1 interact with DDB1, and their binding is enhanced by the phosphorylated N-terminal domain of CUL4B. Finally, a human forebrain organoid model demonstrated that CUL4B is required to develop stable ventricular structures that correlate with onset of forebrain differentiation. Together, our study uncovers previously unrecognized DCAFs relevant for mitosis and brain development that specifically bind CUL4B, but not the CUL4B-P50L patient mutant, by a phosphorylation-dependent mechanism.

Keywords Cullin 4B; cytoskeleton regulation; mitosis; phosphorylation; ubiquitin–proteasome system

Subject Categories Cell Cycle; Post-translational Modifications & Proteolysis

DOI 10.15252/embj.2022112847 | Received 17 October 2022 | Revised 31 May 2023 | Accepted 13 June 2023 | Published online 27 June 2023

The EMBO Journal (2023) 42: e112847

See also: **A Baxi & A Werner** (September 2023)

Introduction

Cullin-RING E3 ligases (CRLs) comprise the largest family of RING-based E3 ubiquitin ligases and catalyze approximately 20% of all ubiquitination reactions leading to proteasomal degradation in mammalian cells (Soucy *et al*, 2009). CRLs use one of eight cullins (CRL1-3, CRL4A-B, CRL5, CRL7, and CRL9) as a scaffolding subunit for their modular assembly. Canonical CRL activity depends on the ubiquitin-like modifier NEDD8 and additional mechanisms altering substrate recruitment, highlighting the high complexity of CRL regulation (Skowyra *et al*, 1997; Olma *et al*, 2009; Deshaies *et al*, 2010; Pierce *et al*, 2013).

CUL4-based E3 ligases regulate many cellular activities, including chromatin-associated processes like DNA damage repair (Sugasawa *et al*, 2005; Wang *et al*, 2006; Guerrero-Santoro *et al*, 2008; Fischer *et al*, 2011) and cell cycle progression (Jin *et al*, 2006; Nishitani *et al*, 2006; Mouysset *et al*, 2015; Gilberto & Peter, 2017). CRL4 complexes engage DDB1-CUL4 associated factors (DCAFs) as substrate receptors (SRs), which are generally characterized by WD40 domains and a helix–loop–helix motif mediating their binding to the adaptor DDB1 (Lee & Zhou, 2007; Fischer *et al*, 2011). Interestingly, vertebrates encode two conserved paralogs, CUL4A and CUL4B, with *CUL4B* gene located on the X-chromosome. The paralogs share over 80% sequence identity, and all functional domains fold into nearly identical structures.

However, CUL4B contains a unique, extended N–terminus, which is mostly unstructured and thus commonly truncated in biochemical

1 Institute of Biochemistry, ETH Zurich, Zurich, Switzerland
2 Brain Research Institute, University of Zurich, Zurich, Switzerland
3 Department of Biosystems Science and Engineering, ETH Zurich, Basel, Switzerland
4 Institute of Molecular Biology, Mainz, Germany
5 Institute of Molecular Systems Biology, ETH Zürich, Zürich, Switzerland
6 Institute of Developmental Biology and Neurobiology (IDN), Johannes Gutenberg University, Mainz, Germany
*Corresponding author. Tel: +41 44 633 65 86; E-mail: matthias.peter@bc.biol.ethz.ch
†These authors contributed equally to this work
‡Present address: Monte Rosa Therapeutics, Basel, Switzerland
§Present address: Faculty Unit of Toxicology, CURML, Faculty of Biology and Medicine, University of Lausanne, Lausanne, Switzerland

studies (Fischer *et al*, 2011, 2014). As both cullins are widely expressed and use DDB1 to bind a common set of SRs, CRL4A and CRL4B complexes are described to have redundant functions (Sugasawa *et al*, 2005; Higa *et al*, 2006; Li *et al*, 2017). Nevertheless, several studies report CRL4A- or CRL4B-specific functions in diverse cellular contexts (Hannah & Zhou, 2015). Indeed, while targeted mass spectrometry (MS) quantification confirmed that CUL4A and CUL4B equally interact with most previously identified DCAFs, a small subset was found to preferentially bind CRL4A or CRL4B complexes. For example, CRBN prefers to assemble with CRL4A, while AMBRA1 favors CRL4B (Reichermeier *et al*, 2020). However, the underlying reason for this DCAF preference is not understood.

Distinct functions of CRL4A and CRL4B complexes are also apparent from studies in mice. CUL4B is essential during mouse embryogenesis, since deletion leads to cell cycle defects and apoptosis in extra-embryonic tissues (Jiang *et al*, 2012; Liu *et al*, 2012b). CUL4A knockout mice, however, show no effects on embryonic viability but fail spermatogenesis (Kopanja *et al*, 2011; Yin *et al*, 2011). Moreover, CUL4B knockouts in mouse epiblasts identified specific neuronal and behavioral defects (Chen *et al*, 2012). In line with these findings, mutations in human CUL4B but not CUL4A are associated with X-linked intellectual disability (XLID; Cabezas *et al*, 2000; Tarpey *et al*, 2007; Vulto-van Silfhout *et al*, 2015; Zou *et al*, 2007), consistent with nonredundant functions of the two cullin scaffolds in brain development (Liu *et al*, 2012a). While most XLID patient mutations result in loss of CRL4B ligase activity, a single point mutation of CUL4B (P50L) mapping to its unique N terminus also causes XLID (Vulto-van Silfhout *et al*, 2015), but the underlying molecular mechanism remains unclear.

Here, we examined the differential roles of CUL4A and CUL4B in cell cycle progression. We found that cells lacking CUL4B show mitotic spindle positioning defects and reduced cortical tension. Molecular analysis revealed that CUL4B is specifically phosphorylated during mitosis and that phosphorylation increases CUL4B interaction with many actin regulators and two previously unrecognized DCAFs, LIS1 and WDR1. Indeed, cells expressing phosphorylation-defective CUL4B mutants including the patient-derived XLID mutant P50L exhibit mitotic defects and the mutant proteins fail to interact with LIS1 and WDR1 *in vivo*. Importantly, *in vitro* reconstitution experiments confirm that LIS1 and WDR1 not only bind DDB1 but also require a second, phosphorylation-dependent interface with the unique amino-terminal domain of CUL4B. Human forebrain organoids formed without CUL4B develop aberrant ventricular structures, implicating CUL4B in early brain development. Our study thus provides a molecular mechanism explaining CRL4B specificity and identifies a previously unrecognized subset of DCAFs that bind CUL4B in a phosphorylation-dependent manner during mitosis.

Results

CRL4B-specific functions in mitosis

To investigate functional differences between CRL4A and CRL4B (Fig 1A), we used RNAi to knock down either CUL4A, CUL4B or DDB1 in HeLa Kyoto cells, with specific downregulation verified by immunoblotting. The neddylation-specific bands of CUL4A and CUL4B were confirmed by CSN (CSN5i-3) and NAE (MLN4924) inhibitor treatment (Figs 1B and EV1A). Upon DDB1 RNAi depletion, CUL4A and CUL4B accumulated predominantly in their deneddylated, inactive form. In contrast, neddylated CUL4A accumulated upon depletion of CUL4B, and conversely neddylated CUL4B increased with CUL4A depletion, implying a potential compensation mechanism (Fig 1C). Despite this paralog compensation, MTT assays revealed decreased growth rates of approximately 30% for CUL4A and 20% for CUL4B RNAi downregulation, respectively, compared with control cells (Fig 1D). The growth rate of CRISPR/Cas9 CUL4B knockout cells (ΔCUL4B) was similarly reduced (Fig EV1B–D). This growth delay phenotype was enhanced to 40–50% when combining CUL4A and CUL4B depletion or upon the depletion of the common adaptor DDB1 (Fig 1D).

Since CRL4 E3 ligase activity is important in DNA replication and DNA damage repair (Wang *et al*, 2006), we hypothesized that the growth delay might in part be caused by accumulation of DNA damage. Indeed, the number of cells positive for phosphorylated histone H2A.X (γH2A.X) increased more than 10-fold following CUL4A depletion (Fig 1E). Similarly, γH2A.X staining by immunofluorescence showed an increase of approximately 25% in cells RNAi-depleted for CUL4A (Figs 1F and EV1E). In contrast, γH2.AX levels in CUL4B-depleted or ΔCUL4B cells were unchanged relative to wild-type controls (Figs 1E and F, and EV1F and G), implying that the observed growth delay is caused by a distinct CRL4B function, independent of DNA damage accumulation.

We next used bright-field live-cell microscopy to visualize division of cells lacking CUL4A or CUL4B. Interestingly, cells lacking CUL4B exhibit a significant lengthening of mitotic duration, which was not observed in CUL4A-depleted or control cells (Figs 1G and EV1H). Indeed, cells with impaired CRL4B took on average 15–25 min longer compared with control cells when measured from rounding-up upon mitotic entry until the onset of cytokinesis. Consequently, we hypothesized a CRL4B-specific function during mitosis as a possible cause for the observed growth delay of CUL4B-depleted cells. Taken together, these results suggest that CRL4B has a unique function that is important for the efficient execution of mitosis, explaining the observed growth delay of CUL4B-depleted cells.

The P50L patient mutation alters mitotic-specific phosphorylation of CUL4B's unique N-terminal extension

We examined CUL4B expression and localization through the cell cycle. As expected, CUL4A and CUL4B are expressed throughout the cell cycle, and their neddylated, active forms are present at all stages. However, when cells were arrested in mitosis either by taxol or nocodazole, CUL4B migrated significantly slower on SDS–PAGE (Fig 2A), indicative of a post-translational modification. Indeed, slower-migrating CUL4B species were readily reversed by incubating mitotic extracts with lambda phosphatase (λ-PP), suggesting CUL4B phosphorylation (Fig 2B). No obvious upshift of the CUL4A band indicative of phosphorylation could be detected, nor when CUL4B was analyzed in extracts prepared from cells arrested in S-phase with thymidine or G2 with RO-3306. CUL4B phosphorylation was also monitored after a mitotic shake-off in asynchronized cells (Fig 2C) or in cells released from a G2 block, thus synchronously progressing from G2 into mitosis (Fig EV2A). In both cases, slower-migrating CUL4B was observed, demonstrating that CUL4B but not CUL4A is specifically phosphorylated during mitosis. Moreover,

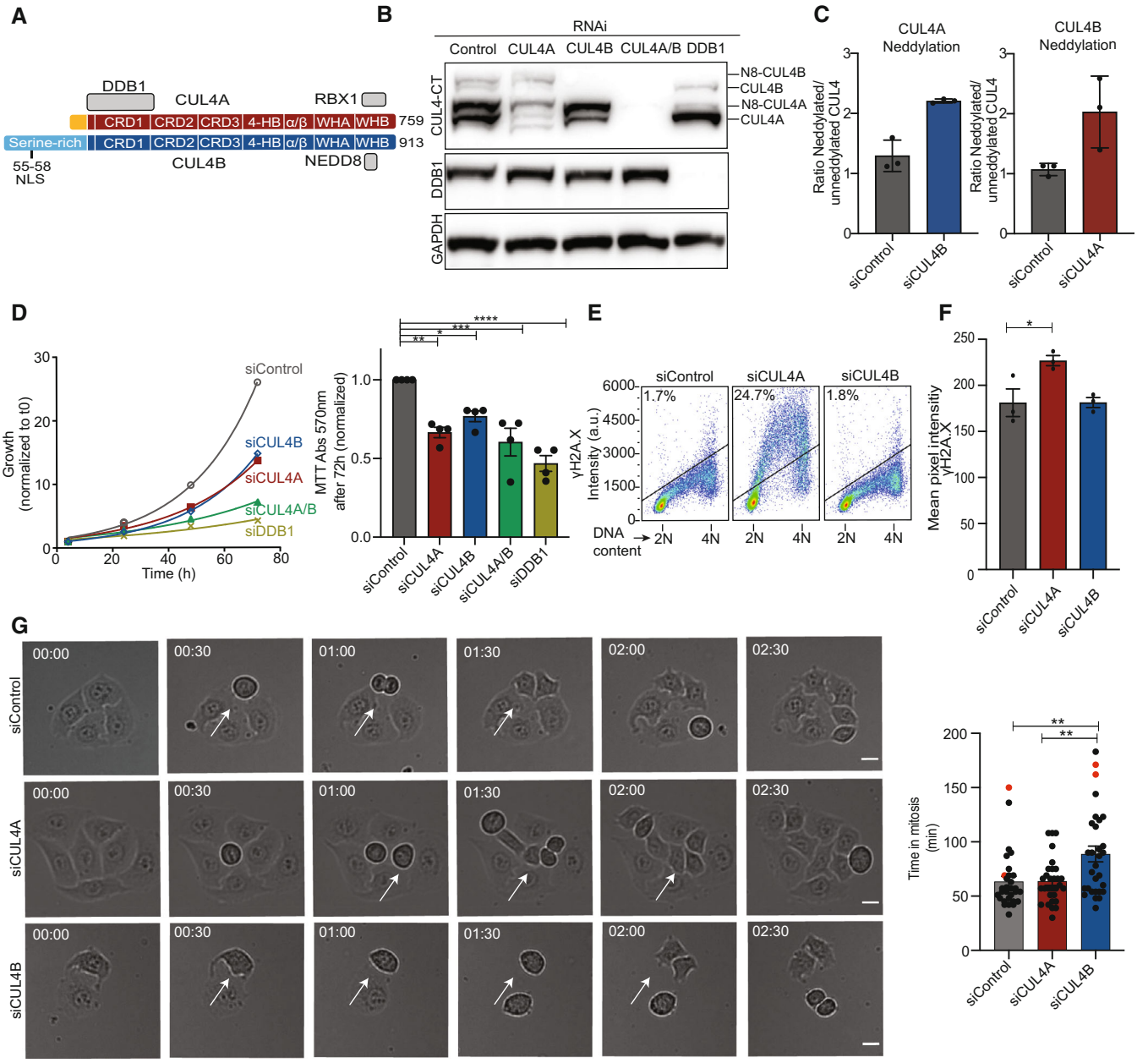

Figure 1. CUL4B-specific functions in mitosis.

A Schematic representation of structural and functional domains of CUL4A (top, red) and CUL4B (bottom, blue) following the annotation described previously (Fischer *et al*, 2011). The common CRL4 subunits and their binding sites are indicated in gray.

B Western blot of RNAi efficiency and specificity for oligos used in (C–G). HeLa Kyoto cells were incubated for 72 h with control oligos or RNAi-oligos depleting CUL4A, CUL4B or DDB1. Specific downregulation of the indicated proteins was analyzed by immunoblotting. GAPDH controls for equal loading.

C Quantification of western blot bands and the ratio between neddylated vs unneddylated CUL4 with the paralog downregulated is calculated. Graphs displays mean with SEM of three biological replicates.

D Growth curves and growth rates of RNAi-depleted HeLa Kyoto cells measured by MTT assay. Graph represents mean with SEM after 72 h normalized to siControl of four biological replicates. $^{****}P < 0.0001$; $^{***}P < 0.001$; $^{**}P < 0.01$; $^{*}P < 0.05$.

E Flow cytometry analysis of Hela Kyoto cells treated with the indicated RNAi for 72 h and immune-stained for γH2A.X and DNA. One of three biological replicates is represented.

F DNA damage levels analyzed by immunofluorescence staining of γH2A.X in RNAi-depleted HeLa Kyoto cells. Quantification of mean pixel intensity of γH2A.X signal in the nucleus. Graph displays mean with SEM of three biological replicates of 150 cells in each experiment. $^{*}P < 0.05$.

G Live-cell imaging of mitosis in RNAi-depleted HeLa Kyoto cells. Bright-field images were taken every 3 min, and mitotic duration was quantified by measuring the time from cell rounding to telophase. Mean with SEM is depicted from three biological experiments analyzing a total of 30 single cells. $^{ns}P = 0.9995$; $^{**}P = 0.0040$; $^{**}P = 0.0044$. Red symbols mark incomplete mitotic events during the movie. White arrows mark cells undergoing mitosis. Scale bar: 10 μm. See Movies EV1–EV3.

Data information: Statistical analysis for all graphs was performed with either *t*-test or 1-ANOVA and Dunnett's multiple comparison. See also Fig EV1.
Source data are available online for this figure.

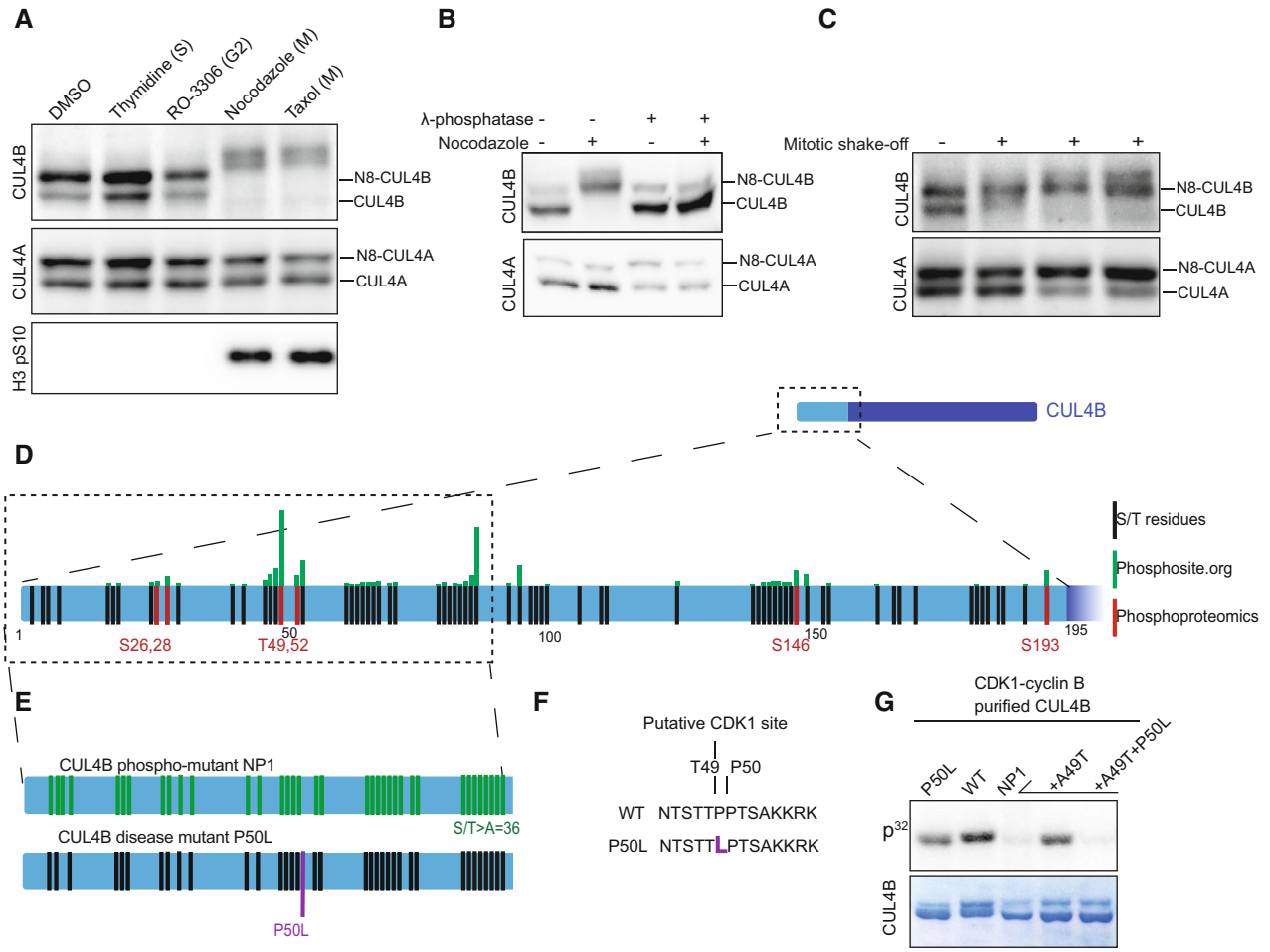

Figure 2. N-terminal phosphorylation of CUL4B during mitosis.

A CUL4A and CUL4B were analyzed by immunoblotting of extracts prepared from HeLa Kyoto cells arrested in S-phase (S = thymidine), G2 (RO-3306), or mitosis (M = nocodazole or taxol). One of three biological replicates is shown. H3 pS10 (phosphorylated histone H3 at serine 10) was used as a mitotic marker. Same samples but separate blot for H3pS10 staining due to size differences.

B Immunoblot of CUL4A and CUL4B extracts prepared from asynchronous (Asyn) or nocodazole (Noc)-arrested mitotic cells were untreated, or treated with λ-phosphatase. One of three biological replicates is shown.

C Mitotic population of unperturbed cells was harvested by shake-off. Three subsequent harvests are depicted (R1-R3). The interphase population are cells that remained attached to the culture dish.

D Black lines mark the serine and threonine residues on the N–terminus of CUL4B. Green lines represent phosphosites found on Phosphosite.org; the green line length indicates the number of studies identifying the site. The red sites were identified by phosphoproteomics on immunoprecipitated HA-CUL4B from nocodazole-arrested mitotic cells. $N = 2$ biological replicates. All sites reported by phosphoproteomics have a localization probability > 0.75 except T52 (0.68).

E Representation of CUL4B amino-terminal mutants used in this study. In the NP1 mutant the green serine and threonine residues located in the first 90 amino acids were mutated to nonphosphorylatable alanine. The P50L XLID patient mutation is highlighted in purple (Vulto-van Silfhout *et al*, 2015).

F Representation of the putative T49 CDK1 consensus site in WT CUL4B, which is altered in the P50L mutant.

G *In vitro* kinase assays with purified CDK1-cyclinB and Sf9-purified CUL4B and mutant proteins in the presence of [γ-^{32}P] ATP. The autoradiogram (top panel) shows CUL4B phosphorylation, while Coomassie staining (lower panel) controls equal loading of CUL4B and mutants ($N = 3$ technical replicates for WT, P50L; NP1; $N = 2$ for NP1-A49T and NP1-A49T-P50L). Note that the A49T mutation in the NP1 mutant restores phosphorylation of the T49 residue, but only in the presence of the adjacent proline at position 50. See also Fig EV2.

Source data are available online for this figure.

phosphorylation sites during mitosis were contained in the unique N terminus of CUL4B, since deletion of the unique N terminus of CUL4B abolished the phosphorylation of CUL4B (Fig EV2B).

Searching the phosphosite.org database revealed many phosphosites located in the unique amino-terminal extension of CUL4B (Fig 2D). To systematically identify the mitotic phosphorylation sites, we immunoprecipitated CUL4B from mitotic cells and mapped phosphorylated peptides after TiO_2 enrichment using MS. To facilitate efficient immunoprecipitation without overexpression, we replaced endogenous CUL4B with a functional HA-tagged CUL4B fusion (Fig EV2C and D). Phosphosite enrichment and quantitative mass spectrometry identified several sites (S26,28; T49,52; S193) in the unique N–terminus of CUL4B, which are phosphorylated during mitosis (Fig 2D; Dataset EV1). T49 conforms to the minimal

consensus site for proline-directed kinases such as cyclin-dependent kinases (CDKs; Fig 2E and F). Indeed, *in vitro* kinase assays in the presence of [γ-^{32}P]ATP demonstrated that purified CUL4B, but not CUL4A, was readily phosphorylated by CDK1-cyclin B, and to a lesser extent also by PLK1 and CK1 (Fig EV2E). Since T49 is located next to the P50L mutation found in XLID patients, we also performed CDK1 *in vitro* kinase assays using purified recombinant CUL4B-P50L as a substrate. In addition, we analyzed a purified recombinant CUL4B mutant (NP1) that has all serine and threonine sites within the first 90 amino acids of the N terminus mutated to nonphosphorylatable alanine residues (Fig 2E). Indeed, CDK1-mediated phosphorylation of the P50L mutant was reduced compared with wild-type (WT) and almost abolished with the NP1 mutant (Fig 2G). Importantly, readdition of the T49 phosphosite to the NP1 mutant partially restored a P^{32} signal, while T49 phosphorylation was strongly reduced when combined with the P50L mutation. We conclude that the unique amino-terminal extension of CUL4B is phosphorylated on multiple sites during mitosis and that CDK1-cyclin B is the main CUL4B kinase *in vitro*. Moreover, phosphorylation of the mitotic CUL4B phosphosite T49 is strongly diminished by the P50L patient mutation (Fig 2G).

Mitotic CUL4B phosphorylation promotes progression through mitosis and regulates chromatin association

In CUL4B knockout HeLa Flp-in cells ($\Delta CUL4B_{Flp}$), we quantified mitotic duration when complemented with inducible expression of CUL4B WT, or the phosphorylation-defective mutants P50L or NP1 by live-cell microscopy. The NP1 and P50L mutant proteins were expressed at comparable levels, while expression of CUL4B WT was slightly lower (Fig 3A). However, expression of both phosphorylation-defective mutants NP1 and P50L failed to rescue the mitotic delay of cells lacking CUL4B, and mitotic duration remained around 90 min in contrast to 60 min observed for CUL4B WT controls (Figs 3B and EV3A). Together, these results demonstrate that mitotic CUL4B phosphorylation and in particular the T49 site is important for mitotic function.

To test the underlying mechanism, we used immunofluorescence to compare chromatin recruitment of endogenous CUL4A and CUL4B during the cell cycle. To simultaneously observe the two CUL4 variants, we used the endogenously HA-tagged CUL4B cell line and co-stained with antibodies specific for CUL4A and the HA-tag. We also employed pre-extraction to deplete the soluble pool of CUL4. While both CUL4A and HA-CUL4B are present in the nucleus (i.e., chromatin-bound) during interphase, we observed a twofold reduction of CUL4B signal on mitotic chromatin, while the CUL4A signal slightly increased at the chromatin in metaphase cells (Fig 3C). Cellular fractionation assays of asynchronous or mitotic cells consistently showed that CUL4B was excluded from mitotic chromatin, while CUL4A remained bound to chromatin throughout mitosis. Chromatin recruitment for CUL4A and CUL4B was abolished after RNAi of DDB1 (Fig EV3B), consistent with earlier reports that CRL4 chromatin recruitment is mediated via specific substrate receptors like DDB2 or RepID (Dai & Wang, 2006; Jang *et al*, 2018).

To test whether exclusion of CUL4B from mitotic chromatin is due to phosphorylation, we used endogenously HA-tagged CUL4B mutant cell lines (Fig 3D). Immunofluorescent staining after cytoplasmic pre-extraction revealed that a N-terminal truncated mutant of CUL4B (ΔN) remains bound to chromatin, comparable to CUL4A localization. Likewise, the NP1 mutant is partially retained, but no chromatin dissociation defect could be detected for the P50L mutant (Fig 3E). Cellular fractionation assays of mitotic cells transiently expressing FLAG-tagged CUL4B, or the two phospho-mutants confirmed slight retention of the NP1 mutant, while the P50L mutant dissociated from mitotic chromosomes comparable to CUL4B WT (Fig EV3C). We conclude that while phosphorylation of the unique amino-terminal domain triggers the dissociation of CUL4B from mitotic chromosomes, this effect cannot solely explain the function of CUL4B in regulating mitosis. Whenever tested, CUL4B mutations found in XLID patients decrease CRL4B abundance and/or activity. Because we have not observed appreciable differences in abundance for CUL4B-P50L with the endogenous promoter (Fig 3D), we examined whether this mutation impacts CRL4 activity. We also examined the phosphorylation-defective NP1 mutant and compared against the neddylation-defective CUL4B-K895R and the L864Afs*13 disease mutant, which severely quench CRL4 activity. We monitored lenalidomide-induced CKIα ubiquitination to quantify $CRL4B^{CRBN}$ activity *in vitro*. As shown in Fig 3F, no significant difference in CKIα ubiquitination kinetics could be detected between CRL4B WT, P50L or NP1 mutants and CRL4A, implying that the P50L nor the engineered NP1 mutant affect the canonical activity of CRL4B. In contrast, the L864Afs*13 disease mutant strongly decreased CKIα ubiquitination, while ubiquitination activity of the CUL4B-K895R mutant was completely abolished. Taken together, these data argue that while the P50L and NP1 phosphorylation-deficient mutants do not prevent CRL4B E3 ligase activity, their inability to rescue CUL4B WT depletion is a strong indicator for a specific role triggered by its phosphorylation state.

LIS1 and WDR1 function as unconventional, phospho-dependent CRL4B DCAFs during mitosis

We hypothesized that phosphorylated CUL4B perhaps assembles distinct E3 ligase complexes to regulate mitotic progression. To identify proteins interacting with CUL4B in a phosphorylation-dependent manner during mitosis, we set up a SILAC-based MS approach (Fig 4A). Briefly, endogenous HA-tagged CUL4B or the phosphorylation-defective P50L or NP1 mutants were immunoprecipitated from SILAC-labeled cells arrested in mitosis with nocodazole. DCAF exchange during lysis was inhibited by blocking the NEDD8 cycle by the addition of the CSN- (CSN5i-3) and NAE inhibitors (MLN4924; Reichermeier *et al*, 2020). Lysates were immunoprecipitated with HA.II antibodies and mixed before the last wash. Bound proteins were separated by SDS–PAGE and identified by LC–MS/MS. As expected, this approach verified that essential components like NEDD8, DDB1, and RBX1 as well as the SR exchange factor CAND1 bind CUL4B by a phosphorylation-independent mechanism. Likewise, we identified several DCAFs and CUL4A as strong interactors of CUL4B and the phosphorylation-defective mutants, indicating the formation of heterodimers or oligomeric assemblies of CRL4A and CRL4B (Figs 4B and EV4A; Dataset EV2). Importantly, however, this analysis also revealed several proteins particularly enriched in the phospho-specific interactome of CUL4B. Most notably, we discovered LIS1 and WDR1, which interact with WT CUL4B but show reduced binding to phosphorylation-defective P50L or NP1 mutants. Both proteins possess WD40 domains preceded by a putative helix–loop–helix motif characteristic for established DCAFs (Figs 4B and EV4B; Fischer

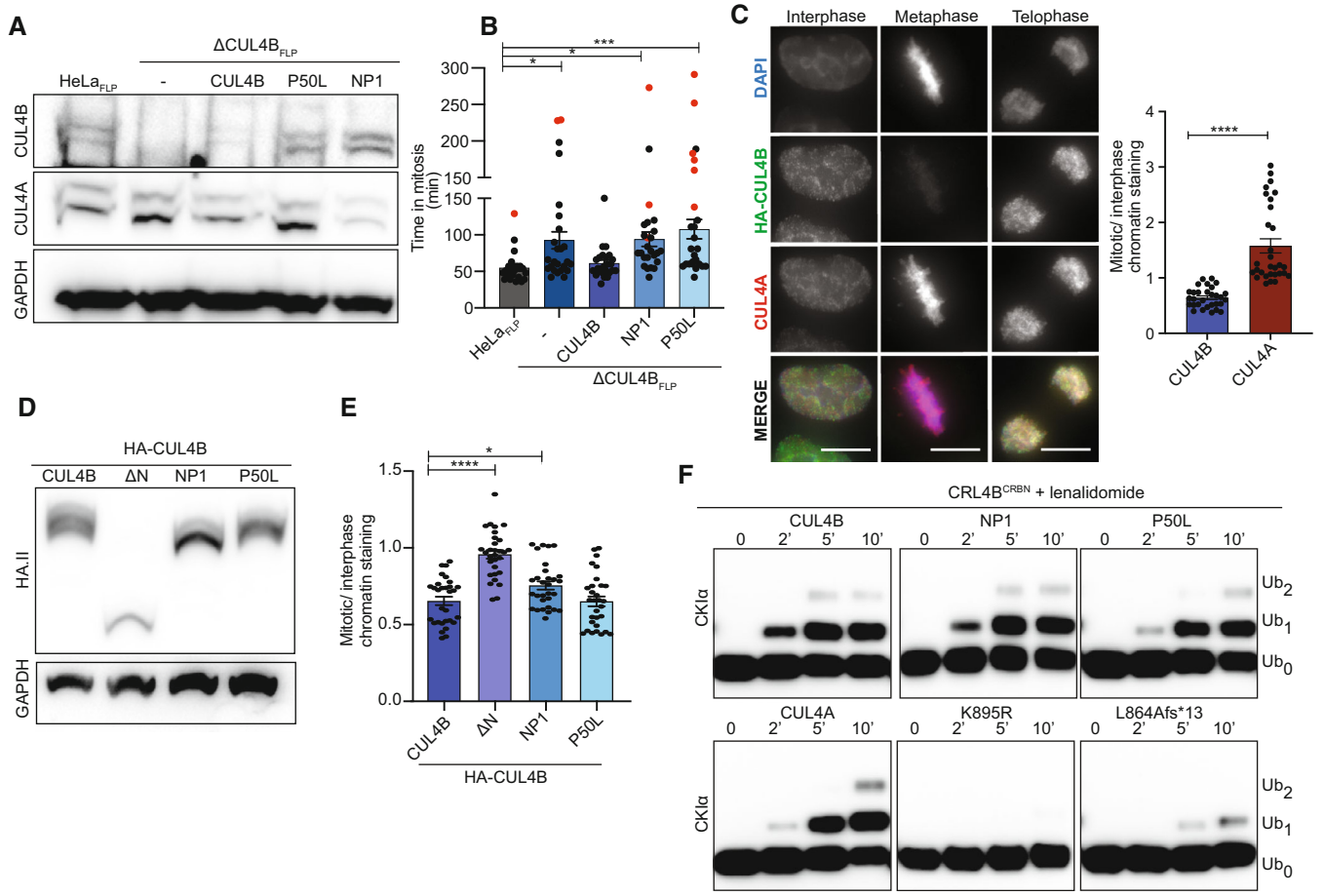

Figure 3. Mitotic CUL4B phosphorylation promotes progression through mitosis and regulates chromatin association.

A Western blot analysis to monitor CUL4A or CUL4B levels in extracts prepared from $HeLa_{FLP}$ control cells or $HeLa_{FLP}$ cells deleted for CUL4B by CRISPR/Cas9 ($\Delta CUL4B_{FLP}$) but stably expressing no CUL4B (−), CUL4B or the indicated NP1 or P50L mutants from the doxycycline-inducible promoter. GAPDH was included to control equal loading. One of three biological replicates is shown.

B Live-cell imaging over time in the bright-field channel from cell rounding to telophase was used to quantify the mitotic duration of $HeLa_{FLP}$ control cells or $\Delta CUL4B_{FLIP}$ cells expressing CUL4B, NP1 or the P50L mutant after doxycycline induction. Mean with SEM is depicted from three biological replicates analyzing a total of 25 single cells. *P = 0.0200; ^{ns}P = 0,9,720; ***P = 0.0005; *P = 0.0147. Red symbols mark cells with incomplete mitosis during image acquisition. See Movies EV6–EV10.

C Immunofluorescence analysis of CUL4A and HA-CUL4B in interphase, metaphase, or telophase cells after cytoplasmic pre-extraction. The DNA was visualized by DAPI. Representative images show maximum intensity Z-projections of the acquired Z-stacks. The contrast settings are identical between images of a single channel. Scale bar: 10 μm. The mean pixel intensity values of HA-CUL4B or CUL4A at a ROI defined as metaphase plates were measured and normalized with ImageJ to mean pixel intensity values of the nuclear signal in interphase nuclei. The graph represents the mean with SEM of three biological replicates with 30 normalized metaphase plates. ****$P < 0.0001$.

D The expression levels of endogenous HA-tagged WT and the indicated CUL4B mutants were compared by immunoblotting with HA.II antibody. GAPDH controls for equal loading.

E Chromatin exclusion of HA-tagged WT and the indicated HA-CUL4B mutants in metaphase was quantified by immunofluorescence after cytoplasmic pre-extraction and normalized with ImageJ to mean pixel intensity values of the nuclear signal in interphase cells. The graph represents the mean with SEM of three biological replicates for 30 normalized metaphase plates. *P = 0.0360; ^{ns}P = 0.9999; ****$P < 0.0001$.

F *In vitro* E3 ligase activity assays using the indicated reconstituted $CRL4B^{CRBN}$ complexes and the neo-substrate CKIα. At time 0, lenalidomide was added to start the reaction and CKIα ubiquitination was followed at the times indicated (in minutes) by immunoblotting with CKIα antibody. $N \geq 3$ technical replicates for CUL4B, CUL4A, P50L, K895R and L864fs*13; $N = 1$ for NP1. Note that the *in vitro* E3 ligase activity of CRL4B and the P50L patient mutation is comparable.

Data information: Statistical analysis was performed with 1-ANOVA and Dunnett's multiple comparison or *t*-test. See also Fig EV3.
Source data are available online for this figure.

et al, 2011; Lee & Zhou, 2007) and may thus function as potential DCAFs specific for phosphorylated CRL4B.

To validate these findings, we focused on three main aspects, namely functional overlap with CUL4B during mitosis, as well as mitosis- and phosphorylation-specific binding. To test whether depletion of LIS1 and/or WDR1 can explain the mitotic defects observed in cells lacking CUL4B, we used live-cell imaging to determine mitotic duration. While RNAi depletion of CUL4B and WDR1 was highly efficient, LIS1 knockdown was moderate (Fig 4C). Interestingly, WDR1- and to a lesser extent LIS1-depleted cells were delayed in mitosis, thus phenocopying at least in part CUL4B-depletion (Figs 4D and EV4C). The mitosis-specific interaction of

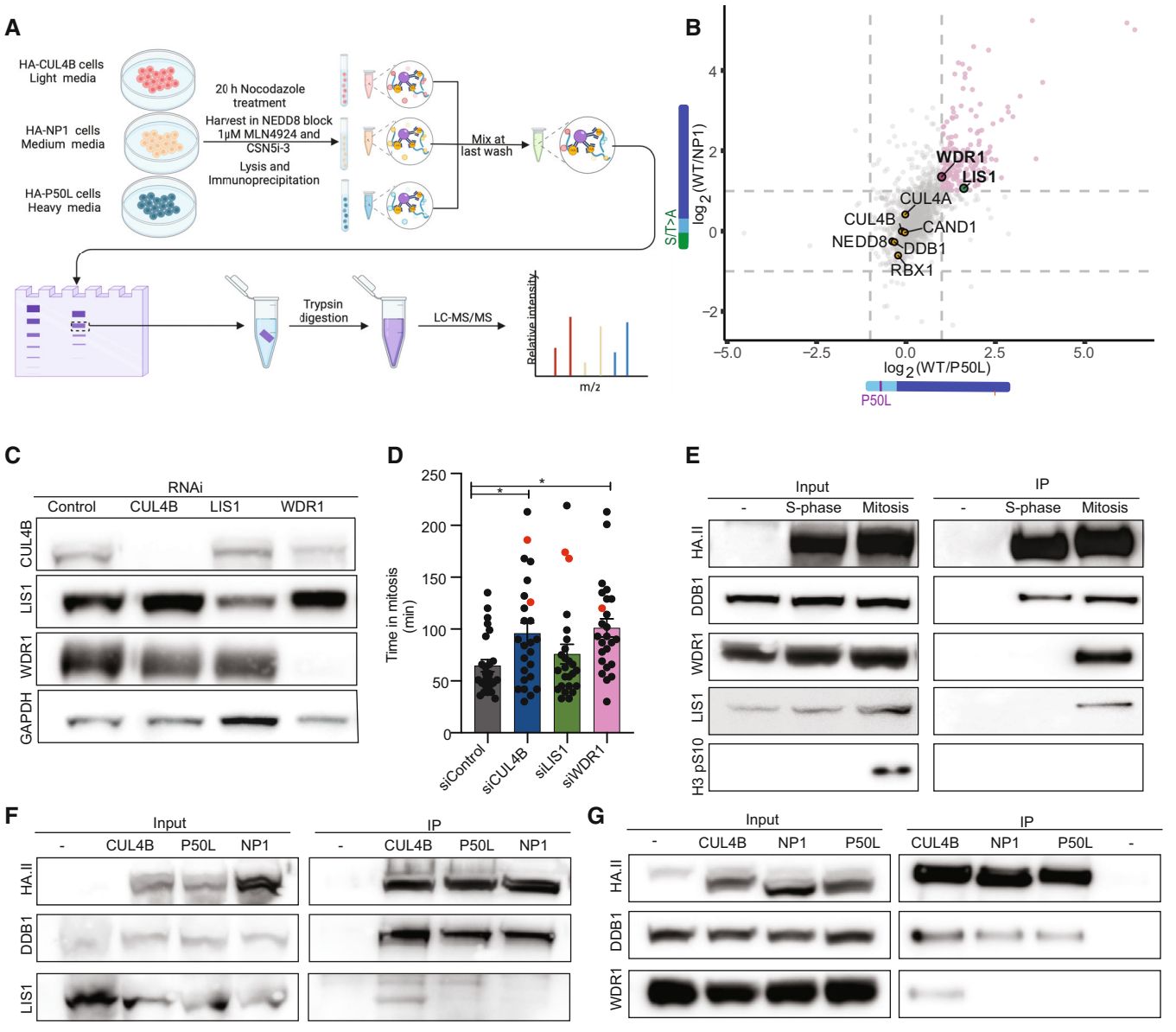

Figure 4. Unconventional DCAFs LIS1 and WDR1 specifically interact with phosphorylated CUL4B during mitosis.

A Outline of the SILAC immunoprecipitation experiment. HeLa Kyoto cells endogenously expressing HA-tagged WT CUL4B or the NP1 or P50L mutants were labeled with heavy, medium, or light SILAC medium and arrested in mitosis with nocodazole for 20 h. Cell lysis was performed in the presence of the CSN inhibitor CSN5i-3 and NAE inhibitor MLN4924 to prevent DCAF exchange. Samples were mixed after immunoprecipitation with HA.II antibodies and bound proteins separated by SDS–PAGE before trypsin digestion and MS-analysis.

B Scatter plot comparing mitotic immunoprecipitations (IP) of phosphorylated CUL4B with the phospho-mutants NP1 and P50L. The axes represent the log2-transformed fold change of WT CUL4B vs mutant IPs, with dashed lines marking 2× fold change cutoffs. Proteins preferentially binding to phosphorylated CUL4B compared with the phosphorylation-defective mutants, such as WDR1 and LIS1, group in the upper right corner.

C To control RNAi efficiency and specificity, HeLa Kyoto cells were incubated for 72 h with control oligos (control) or RNAi-oligos depleting CUL4B, LIS1 or WDR1. Specific downregulation of the indicated proteins was analyzed by immunoblotting. GAPDH controls for equal loading. One of three biological replicates is shown.

D The mitotic duration of siControl cells or cells RNAi-depleted for CUL4B, LIS1 or WDR1 was quantified by life cell microscopy in the bright-field channel measuring the time from cell rounding to telophase. Mean with SEM is depicted of $N = 4$ biological replicates with a total of 25 single cells. *$P = 0.0337$; $^{ns}P = 0.6888$, *$P = 0.0103$. Red symbols mark cells with incomplete mitosis during the movie.

E HA immunoprecipitation (IP) of extracts (input) prepared from unedited (–) or HA-CUL4B endogenously expressing HeLa Kyoto cell lines arrested in S-phase (thymidine) or mitosis (nocodazole) were probed with antibodies against LIS1, WDR1 and DDB1. The antibody recognizing phospho-H3(S19) controls mitotic arrest and specificity of the immunoprecipitation.

F, G HeLa Kyoto endogenously expressing HA-CUL4B or the indicated NP1 or P50L mutants were arrested in mitosis with nocodazole. Extracts (input) and HA immunoprecipitants were analyzed for the presence of HA-CUL4B for control and bound DDB1 and LIS1 (F) or DDB1 and WDR1 (G), respectively. One of three biological replicates is shown.

Data information: Statistical analysis was performed with 1-ANOVA and Dunnett's multiple comparison. See also Fig EV4.
Source data are available online for this figure.

CUL4B with LIS1 and WDR1 was verified by immunoprecipitating HA-tagged CUL4B from cells arrested in S-phase by thymidine or in mitosis with nocodazole (Fig 4E). Phospho-specificity was confirmed by comparing immunoprecipitations of HA-tagged CUL4B and the phosphorylation-defective mutants NP1 and P50L in cells arrested in mitosis by nocodazole. Indeed, these assays demonstrated mitosis-specific binding of CUL4B to LIS1 and WDR1, which was not observed when analyzing the phosphorylation-defective mutants NP1 and P50L (Fig 4F and G). Together, these results suggest that LIS1 and WDR1 function as phospho-specific DCAFs (pDCAF), assembling with phosphorylated CRL4B (pCRL4B) to regulate progression through mitosis.

LIS1 and WDR1 binding is mediated via two different binding sites, one on DDB1 and one on CUL4B

We next used reconstituted complexes (DDB1, RBX1 and either CUL4A or CUL4B) and established a fluorescence polarization (FP) assay to dissect binding affinities of LIS1 and WDR1 to different CRL4 subunits. Since LIS1 and WDR1 possess helix–loop–helix motifs predicted to mediate DDB1 binding, we also performed pull-down experiments using LIS1, WDR1 or for control DCAF8 from *Sf9*-extracts co-expressing DDB1. Indeed, both LIS1 and WDR1 specifically interact with DDB1 under these conditions, although with weaker affinity compared with the conventional DCAF8 (Figs 5A and EV5A). FP assays confirmed that these interactions are direct and revealed that LIS1 and WDR1 bind DDB1 with a Kd of approx. 5 μM (Fig 5B). FP assays confirmed that LIS1 and WDR1 bind DDB1 with a K_d of approx. 5 μM (Fig 5B). As expected, deletion of the N-terminal region of LIS1, which includes the predicted HLH motif, abrogates binding to DDB1 (Fig EV5B). In contrast, deleting the first 29 amino acids of WDR1 was not sufficient to disrupt DDB1 binding (Fig EV5B), consistent with an AlphaFold model indicating that the predicted HLH-box is at the interface between the two WD40 domains and is thus an integral part of the second WD40-repeat domain. Interestingly, we also detected interaction of LIS1 (FL) and WDR1 (FL) with CUL4B after co-expression in Sf9 cells in the absence of DDB1. This implies two distinct binding sites of LIS1 and WDR1, one on DDB1 and another one on the N–terminus of CUL4B (Fig 5C and D). Consistent with this hypothesis, purified LIS1 and WDR1 preferentially interacted with CRL4B compared with CRL4A, which lacks the N-terminal extension (Figs 5E and F, and EV5C and D). Strikingly, LIS1 and WDR1 exhibit a pronounced binding preference to CRL4B with a K_d around 1 μM, while binding to CRL4A is almost undetectable (K_d around 13 μM; Figs 5G and H, and EV5E).

To investigate whether phosphorylation may enhance the amino-terminal interaction, we first compared CRL4B purified from *Sf9* cells, after additional treatments with either CDK1 or λ-PP. While incubating *Sf9*-expressed CUL4B by CDK1 ($CRL4B_{CDK1}$) did not alter its migration on SDS–PAGE, λ-PP treatment ($CRL4B_{\lambda\text{-}PP}$) led to a faster migrating CUL4B band, similar to the phosphorylation-defective NP1 mutant ($CRL4B_{NP1}$) (Fig EV5F), arguing that purified WT CUL4B is phosphorylated. We thus measured the binding affinity of LIS1 or WDR1 to *Sf9*-purified CRL4B with or without λ-PP treatment. Indeed, dephosphorylation of CRL4B reduced its binding affinity to LIS1 and WDR1 at least fourfold, reaching the affinity observed by direct DDB1 binding (Fig 5I and J). To corroborate these data, we also performed *in vitro* pull-down assays of purified LIS1 and WDR1 with CRL4B, $CRL4B_{NP1}$, and $CRL4B_{\lambda\text{-}PP}$. While CRL4B binds LIS1 or WDR1 in an almost stoichiometric ratio, we observed decreased binding of LIS1 and WDR1 to $CRL4B_{NP1}$ or

Figure 5. Recruitment of LIS1 and WDR1 into the CRL4B complex is mediated via two different binding sites, one on DDB1 and one on phosphorylated CUL4B.

A Coomassie-stained SDS–PAGE of *in vitro* pull-down assays of FLAG-tagged LIS1 and WDR1, and His-DDB1, co-expressed in baculoviral *Sf9* cells, F is FLAG and H is His. One of three biological replicates is shown. Note that DDB1 specifically interacts with LIS1 and WDR1.

B Fluorescence polarization (FP) assay quantifying direct binding of Alexa-labeled LIS1 ($N = 3$ technical replicates) and WDR1 ($N = 2$ technical replicates) to DDB1 as mean with SD.

C, D Western blot of *in vitro* pull-down assays of Strep-tagged CUL4B and FLAG-tagged LIS1 (C) or WDR1 (D) co-expressed in Sf9 cells in the presence (+) or absence (–) of DDB1. One of three biological replicates is shown. Note that LIS1 and WDR1 specifically bind CUL4B, but this interaction is enhanced by the presence of DDB1.

E Coomassie-stained SDS–PAGE of purified proteins (input) and *in vitro* binding assays (Strep pull-down) of Strep-LIS1 with purified CRL4A or CRL4B. One of three technical replicates is shown. Please note that the 2nd and 3rd lanes of this gel are also shown on EV5F as controls.

F Coomassie-stained SDS–PAGE of purified proteins (input) and *in vitro* binding assays (Strep pull-down) of Strep-WDR1 with purified CRL4A or CRL4B. One of two technical replicates is shown.

G FP assay investigating binding of CRL4B and CRL4A to Alexa-labeled LIS1. The mean with SD of three technical replicates is shown from independent purifications of CRL4B.

H Fluorescence polarization assay investigating the binding of CRL4B and CRL4A to Alexa-labeled WDR1 ($N = 3$ technical replicates).

I Fluorescence polarization assay comparing the binding of CRL4B and λ-PP-treated CRL4B to Alexa-labeled LIS1. The mean with SD of three technical replicates is depicted.

J Fluorescence polarization assay comparing the binding of CRL4B and λ-PP-treated CRL4B to Alexa-labeled WDR1. The mean with SD of three technical replicates is depicted.

K Quantification of *in vitro* binding assays (Strep pull-down) of Strep-LIS1 with purified CRL4B, the NP1 phospho-mutant ($CRL4B_{NP1}$) ($N = 3$ technical replicates), or λ-PP-treated (dephosphorylated) CRL4B ($CRL4B_{\lambda\text{-}PP}$) ($N = 2$ technical replicates).

L Quantification of *in vitro* binding assays (Strep pull-down) of Strep-LIS1 with purified CRL4B, or the NP1 phospho-mutant ($CRL4B_{NP1}$) ($N = 2$ technical replicates), or λ-PP-treated CRL4B ($CRL4B_{\lambda\text{-}PP}$) ($N = 1$).

M Schematic model visualizing the assembly of phospho-specific DCAFs (pDCAF)-containing E3 ligase complexes with N-terminally phosphorylated CRL4B during mitosis. Band intensities were quantified and normalized to LIS1 and WDR1, respectively.

Data information: Statistical analysis: One site-specific binding of saturation binding. Note that LIS1 and WDR1 preferentially bind to phosphorylated CRL4B. The three panels Figs 5E and EV5G and F originate from the same Coomassie gel, but each cropped group of lanes conveys a different message. Overlapping lanes were used as controls.
Source data are available online for this figure.

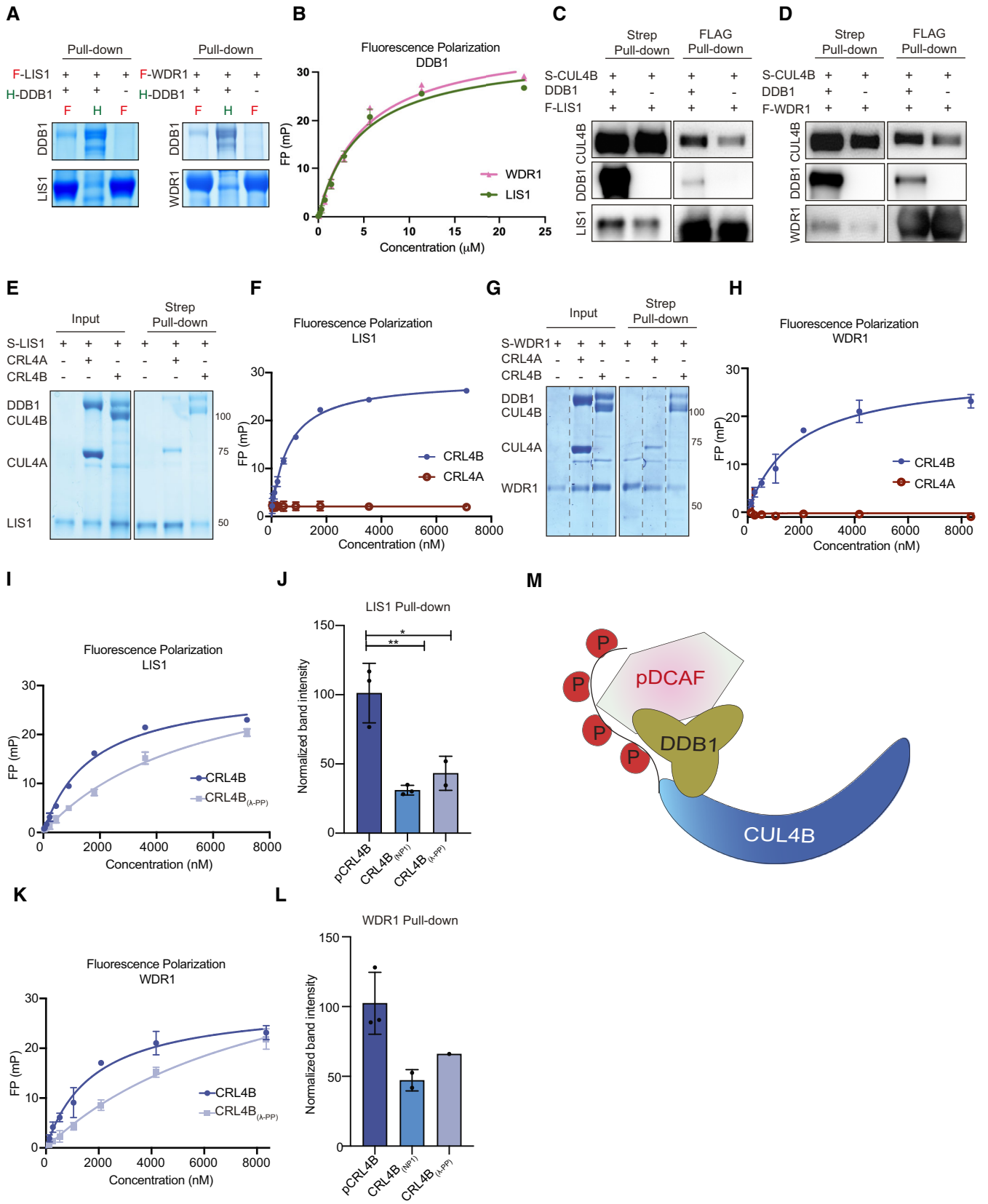
A
Pull-down
F-LIS1 + + +
H-DDB1 + + -
F H F
DDB1
LIS1
Pull-down
F-WDR1 + + +
H-DDB1 + + -
F H F
DDB1
WDR1
B
Fluorescence Polarization
DDB1
FP (mP)
Concentration (μM)
WDR1
LIS1
C
Strep Pull-down
FLAG Pull-down
S-CUL4B + + + +
DDB1 + - + -
F-LIS1 + + + +
DDB1 CUL4B
LIS1
D
Strep Pull-down
FLAG Pull-down
S-CUL4B + + + +
DDB1 + - + -
F-WDR1 + + + +
DDB1 CUL4B
WDR1
E
Input
Strep Pull-down
S-LIS1 + + + + + +
CRL4A - + - - + -
CRL4B - - + - - +
DDB1
CUL4B
CUL4A
LIS1
100
75
50
F
Fluorescence Polarization
LIS1
FP (mP)
Concentration (nM)
CRL4B
CRL4A
G
Input
Strep Pull-down
S-WDR1 + + + + + +
CRL4A - + - - + -
CRL4B - - + - - +
DDB1
CUL4B
CUL4A
WDR1
100
75
50
H
Fluorescence Polarization
WDR1
FP (mP)
Concentration (nM)
CRL4B
CRL4A
I
Fluorescence Polarization
LIS1
FP (mP)
Concentration (nM)
CRL4B
CRL4B(λ-PP)
J
LIS1 Pull-down
Normalized band intensity
pCRL4B
CRL4B(NPI)
CRL4B(λ-PP)
M
P
P
P
P
pDCAF
DDB1
CUL4B
K
Fluorescence Polarization
WDR1
FP (mP)
Concentration (nM)
CRL4B
CRL4B(λ-PP)
L
WDR1 Pull-down
Normalized band intensity
pCRL4B
CRL4B(NPI)
CRL4B(λ-PP)

Figure 5.

λ-PP-treated CRL4B (CRL4B$_{\lambda\text{-PP}}$) (Figs 5K and L, and EV5G and H). No binding defect was observed when comparing wild-type CUL4B to the P50L mutant by FP assays (Fig EV5I), suggesting that phosphorylation at sites other than T49 contributes to binding the amino-terminal CUL4B extension *in vitro*. Taken together, our results suggest that in addition to DDB1, the phosphorylated N terminus of CUL4B stabilizes the interaction with the pDCAFs LIS1 and WDR1 (Fig 5M).

CRL4B^{LIS1} and CRL4B^{WDR1} complexes regulate cortex tension and spindle positioning during mitosis

Consistent with the reported functions of WDR1 and LIS1 in regulating actin dynamics (Ono, 2018) and the dynein/dynactin complex (Elshenawy *et al*, 2020), respectively, our phospho-specific, mitotic CUL4B interactome revealed multiple proteins involved in cytoskeletal regulation. Indeed, the GO term analysis of the MS dataset found strong enrichment of components involved in cytoskeleton organization and actin filament-based processes (Fig 6A and B; Datasets EV2 and EV3). Interestingly, the Arp2/3 complex was specifically immunoprecipitated by HA-tagged CUL4B in mitosis and its interaction was strongly reduced when analyzing the phosphorylation-defective NP1 and P50L mutants (Fig 6C). Likewise, HA-CUL4B immunoprecipitates prepared from extracts of mitotic cells (Fig 6D) contained actin and dynactin, which are known interactors of WDR1 and LIS1, respectively.

To functionally dissect possible cytoskeletal functions of pCRL4B^{LIS1} and pCRL4B^{WDR1} during mitosis, we RNAi-depleted CUL4B, LIS1, or WDR1 in HeLa cells expressing LifeAct-GFP and H2B-RFP (Matthews *et al*, 2012) and monitored actin dynamics as well as spindle movement and positioning. While we did not detect grossly aberrant actin structures in CUL4B or LIS1 RNAi-depleted cells, we observed severe blebbing and cell death in WDR1-depleted cells. We also used atomic force microscopy (AFM) in a cell confinement assay to assess actin-dependent cortical tension and cell stiffness during mitosis (Fig EV6A). Interestingly, we detected a strong reduction in the initial confinement force (or peak force) in cells lacking CUL4B (Figs 6E and EV6B). Similarly, WDR1 or LIS1 depletion reduced this peak force, although to a lower extent (Fig 6E, left panel). In addition, the tension of the actin cortex was strongly reduced in LIS1 and CUL4B-depleted cells, while WDR1 depletion only led to a small decrease (Fig 6E, right panel). Together, these data indicate that CRL4B activity is required to stabilize the cell cortex during mitosis, most likely by regulating actin-dependent structures via LIS1 and WDR1.

Since LIS1 is known to regulate dynein/dynactin complexes and spindle positioning (Moon *et al*, 2014), we tested whether CUL4B is required for proper spindle organization and function. Indeed, immunofluorescence experiments revealed that ΔCUL4B cells show an increased number of off-centered mitotic spindles (Fig EV6C). To corroborate these findings, we used live-cell microscopy to follow spindle dynamics in single cells. Kymographs showed enhanced spindle mobility in CUL4B-depleted cells and spindle movement increased fivefold compared with controls. Assessment of the spindle angle indicated that the mitotic spindle was not stably anchored to the cortex with an increased mobility in all three dimensions (Fig 6F and G). As expected, similar spindle defects were detected in LIS1-depleted cells, while lack of WDR1 did not significantly alter spindle dynamics (Fig 6F and G). Thus, phenotypic characterization indicates that CRL4B^{WDR1} regulates mitotic duration possibly by actin rearrangements, while CRL4B^{LIS1} is required to stably anchor the mitotic spindle to the cell cortex and increase cortex tension.

Human forebrain organoids to model developmental impact of CUL4B depletion

Since CUL4B mutations impair brain development in human patients (Vulto-van Silfhout *et al*, 2015), we examined CUL4B function in an *in vitro* model of human forebrain development. While CRISPR-mediated deletion of CUL4B (ΔCUL4B) was confirmed by western blot, we did not observe changes in CUL4A protein levels

Figure 6. CRL4B^{LIS1} and CRL4B^{WDR1} E3 ligase complexes may regulate cortex tension and spindle positioning during mitosis.

A Mass spectrometric analysis of HA immunoprecipitants (IP) using extracts prepared from SILAC-labeled, nocodazole-arrested (mitotic) HeLa Kyoto cells endogenously expressing HA-tagged WT CUL4B or the NP1 and P50L phospho-mutants. The workflow is described in Fig 4A, and the data displayed as scatter plot. The axes represent the log2-transformed fold change of phosphorylated WT CUL4B vs mutant IPs, with dashed lines marking 2× fold change cutoff. Proteins preferentially binding to phosphorylated CUL4B cluster in the upper right corner.

B GO term biological process analysis of the interactome preferentially binding to phosphorylated CUL4B vs the NP1 mutant.

C Extracts (input) prepared from S-phase (S; thymidine) or mitosis (M; nocodazole)-arrested HeLa Kyoto cells (–) and endogenously expressing HA-tagged WT CUL4B, or the NP1 or P50L mutants were immunoprecipitated with HA.II antibodies (IP). Bound ACTR3 or DDB1 was detected using specific antibodies. One of three biological replicates is shown. Note that in contrast to DDB1, ACTR3 binds CUL4B in a phosphorylation-dependent manner.

D HA immunoprecipitants (IP) of extracts (input) prepared from unedited (–) controls or endogenously expressing HA-CUL4B HeLa Kyoto cells arrested in mitosis with nocodazole were probed with antibodies against DDB1, DCTN1, (dynactin) and actin. One of two biological replicates is depicted.

E AFM measurements of the peak confinement force (left) and cortical tension (right) in mitotic cells. HeLa Kyoto cells were incubated for 72 h with control oligos (siControl) or RNAi-oligos depleting CUL4B, LIS1, or WDR1. After 30 min of (+)-S-trityl-l-cysteine (STC) treatment, the confinement force was measured for single mitotic cells by AFM. The initial or peak force is displayed as the mean in nano-Newton (nN) with SEM. $N = 2$ biological replicates with a total of 20 single cells. The right panel represents tension during confinement in mN m^{-1} with standard deviation depicted as thin lines for a representative replicate.

F Live-cell imaging of HeLa cells expressing H2B-mcherry and lifeAct-GFP, treated for 72 h with control oligos (siControl) or RNAi-oligos depleting CUL4B, LIS1 or WDR1. Representative cells are shown in time intervals of 6 min during metaphase with identical contrast settings. The unanchored spindle in CUL4B- and LIS1 deleted cells is marked with a white arrow. Scale bar: 10 μm. See also Movies EV11–EV14.

G The mean delta position (left bar graph) and the mean delta angle (right bar graph) with SEM quantifies the average spindle movement (in pixel per time frame) or spindle rotation (in rad). $N = 4$ biological replicates with a total of 25 single cells. ****$P < 0.0001$, ***$P = 0.0004$, $^{ns}P = 0.5306$ and ****$P < 0.0001$; *$P = 0.0110$; $^{ns}P = 0.0242$. Only cells with completed mitosis were measured. The kymographs visualize the spindle movement during metaphase.

Data information: Statistical analysis was performed by 1-ANOVA with Dunnett's multiple comparison with RNAi control. See also Fig EV6.
Source data are available online for this figure.

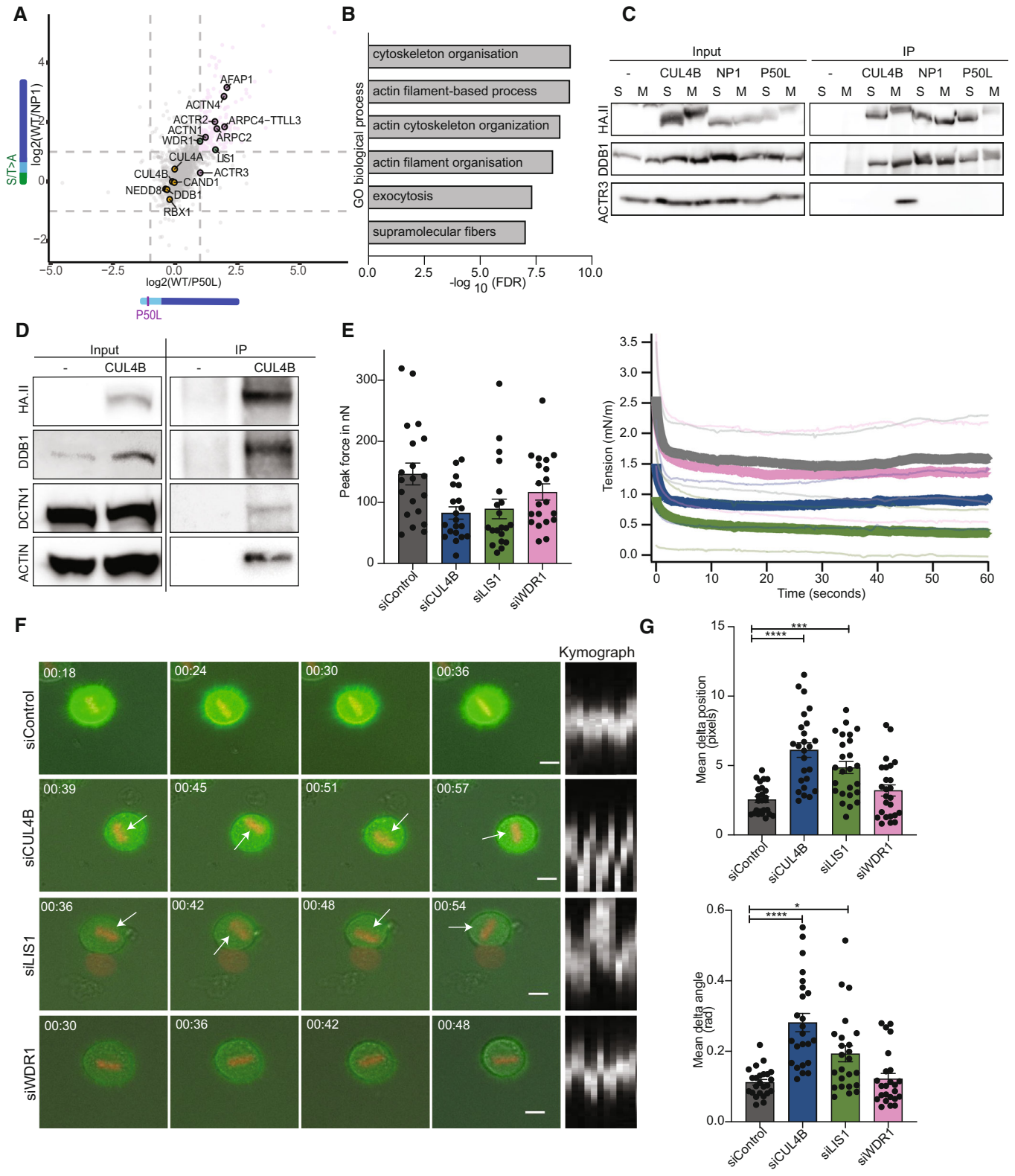

Figure 6.

nor neddylation status (Fig EV7A). Strikingly, human forebrain organoids from ΔCUL4B H9 human embryonic stem cells (H9 hESCs) exhibited a severe loss of ventricular structures by Day 35 (Fig 7A and B). To determine the onset of the ventricular phenotype, we analyzed the structure at the embryoid body stage (Day 6), neuronal tube stage (Day 12) and during neurogenesis (Day 19;

Fig EV7B). This time course experiment revealed that ΔCUL4B organoids can successfully produce ventricles during early organoid formation. However, these ventricles were severely affected shortly after the onset of neurogenesis (Fig EV7C). This phenotype was quantified at Days 6, 12, and 19 by assessing β-catenin-positive ventricles (Fig EV7D). In contrast to previous results (Tripathi *et al*, 2007), we found that the β-catenin-positive ventricles were generally reduced in ΔCUL4B organoids compared with unedited controls. Together, we conclude that CUL4B is specifically required to maintain ventricular structures in human forebrain organoids (Fig 7A and B), consistent with a unique function of CUL4B in human brain development.

Discussion

Our study establishes a novel CRL4B-specific regulatory mechanism comprising cell-cycle-dependent phosphorylation of its unique

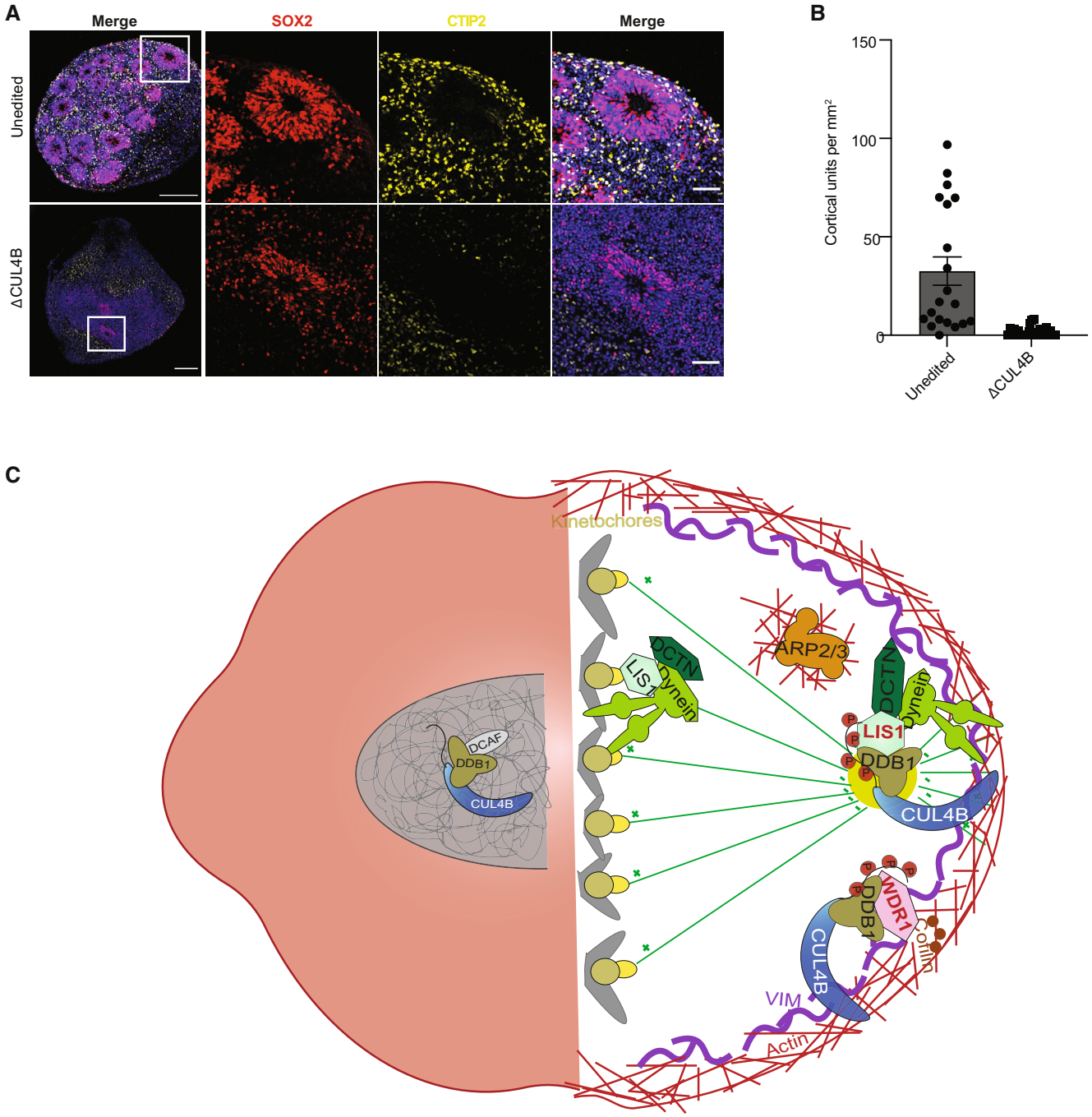

Figure 7.

Figure 7. Analysis of CUL4B function using human forebrain organoids.

Unedited (top row) or CUL4B-deleted (bottom row) H9 hESCs were differentiated to generate human forebrain-specific regionalized organoids. Sections were stained as indicated with antibodies against SOX2 or CTIP2 to visualize neural stem cell and neuronal cell populations, respectively.

A Example images of Day 35 organoids. The stained sections are also shown as merged images at different magnifications, with scale bars of 200 and 50 μm, respectively.

B The number of cortical units per mm^2 total area was quantified in unedited and ΔCUL4B brain organoids at Day 35. Ventricles were counted and the number divided by the total organoid area on 20 sections from one biological replicate. See also Fig EV7.

C Schematic representation of CRL4B in interphase and mitosis. CRL4B phosphorylation during mitosis promotes binding of the phospho-specific DCAFs LIS1 and WDR1, thereby regulating cytoskeletal dynamics during mitosis. The centrosome is shown as yellow circle, and chromatin/chromosomes are depicted in gray. Functions of LIS1 and the dynein/dynactin complex at kinetochores and the cell cortex are highlighted. Green lines represent spindle and astral microtubules and red lines cortical actin filaments, possibly regulated by the Arp2/3 complex and WDR1/cofilin activity. Vimentin (Vim) filaments stabilizing the cell cortex are indicated in violet.

Source data are available online for this figure.

unstructured N-terminal domain. We demonstrate that phosphorylated CUL4B engages with the previously unrecognized DCAFs, LIS1 and WDR1, which together regulate cortex tension and spindle positioning during mitosis. Since the P50L patient mutation is specifically defective for its mitotic phosphorylation and in turn fails to bind LIS1 and WDR1 *in vivo*, our findings provide important insights to understand the molecular mechanisms causing XLID and possibly other human neurological diseases.

We found that the unique CUL4B extension contains many S/T residues, which are phosphorylated during mitosis. Indeed, several mitotic kinases including CDK1, PLK1, or Aurora B phosphorylate CUL4B *in vitro*. CDK1-cyclin B emerged as the major CUL4B kinase preferentially phosphorylating T49, the major site conforming to the minimal S/T-P-X motif (Errico *et al*, 2010; Alexander *et al*, 2011). Strikingly, the P50L XLID patient mutation interferes with phosphorylation of the adjacent T49 residue, explaining its mitotic defect. CDK1 sites often promote PLK1 binding, which then further increases phosphorylation (Elia *et al*, 2003; Watanabe *et al*, 2005). It will be interesting to explore whether nonmitotic kinases may similarly shape appropriate cellular responses by regulating CUL4B function through phosphorylation of its unique amino-terminal domain in response to different environmental conditions.

We found that CUL4B phosphorylation is required for efficient progression through mitosis by two mechanisms (Fig 7C). First, mitotic phosphorylation triggers its dissociation from mitotic chromatin, and second, phosphorylation allows binding of CUL4B to previously unrecognized DCAFs, including WDR1 and LIS1. Both WDR1 and LIS1 possess WD40 domains and bind DDB1 most likely through a helix–turn–helix motif (Lee & Zhou, 2007; Fischer *et al*, 2011). Importantly, however, their interaction is stabilized by a separate binding motif generated by the phosphorylated amino-terminal extension of CUL4B. Together, the two distinct binding sites promote the assembly of stoichiometric CRL4B complexes with low micromolar affinity like conventional DCAFs binding to CRL4s. Biophysical and structural work will be required to understand the underlying properties and deduce critical residues stabilizing the DDB1-LIS1 and DDB1-WDR1 heterodimers bound to phosphorylated CUL4B. It is possible that additional CRL4B-specific DCAFs exist, including unconventional DCAFs which require other modifications of the amino terminus. An interesting candidate could be AMBRA1, which was recently shown to regulate cyclin D degradation via CUL4B (Chaikovsky *et al*, 2021; Maiani *et al*, 2021; Simoneschi *et al*, 2021). Notably, functional importance of the unique N-terminal region of CUL4B was also demonstrated for the Dioxin receptor, which binds independently of DDB1 (Ohtake *et al*, 2007). Moreover, WDR1 was previously reported to function as a DCAF in *Trypanosoma brucei*, which encodes CUL4 with an amino-terminal extension like CUL4B (Hu *et al*, 2017). It will thus be interesting to compare evolutionary conserved features, as the unique amino-terminal extension increases the repertoire of substrate receptors specifically functioning within CRL4B complexes. Our observations may also be relevant for targeted protein degradation, since several degraders rely on substrate recruitment by the $CRL4^{CRBN}$ E3 ligase (Pettersson & Crews, 2019). Exploiting phospho-dependent CRL4B substrate receptors may restrict neo-substrate targeting to proliferating cells in mitosis.

Several studies have addressed molecular functions of LIS1 and WDR1 in mitosis. LIS1 regulates spindle mobility and orientation by regulating the dynein/dynactin complex and by increasing the density of astral microtubules, which may in turn affect cortical tension (O'Connell & Wang, 2000; Quintyne & Schroer, 2002; Moon *et al*, 2014). Cells lacking CUL4B similarly exhibit spindle positioning and cortical tension defects, and it is thus tempting to speculate that $pCRL4B^{LIS1}$ regulates dynein/dynactin activity (Fig 7C). Less is known about the molecular functions of WDR1, but available data suggest that it likely controls the actomyosin network and functions in mitotic cell rounding (Fujibuchi *et al*, 2005; Bowes *et al*, 2019).

While LIS1 and WDR1 coordinately regulate cortical tension and cytoskeletal dynamics, it remains to be examined if and how these cortical defects alter mitotic timing. In mitosis, the cortex becomes thinner with increased tension due to RhoA activation, which allows cells to change to the rounded-up morphology (Maddox & Burridge, 2003). Both spindle orientation and chromosome separation rely on the actomyosin cortex providing a rigid scaffold to counteract the traction forces exerted on astral microtubules by motors pulling toward the spindle poles (Rizzelli *et al*, 2020). Given the overlapping defects of cells lacking CUL4B, LIS1, and WDR1 in cortical tension and cytoskeletal dynamics, the formation of functional $CRL4B^{LIS1}$ and $CRL4B^{WDR1}$ E3 ligase complexes may contribute to these functions during mitosis (Fig 7C). A critical next step to test this exciting hypothesis will be the identification of relevant substrates of mitotic CRL4B complexes. Candidates include proteins directly binding to LIS1 and WDR1, and we indeed found dynactin and many actin regulators as mitotic-specific interactors of CUL4B. Further studies are needed to demonstrate whether these candidates are indeed critical substrates for pCUL4B-dependent ubiquitination.

Our results provide important molecular insight into the function of CRL4B in XLID and related intellectual disability disorders. In

contrast to most *CUL4B* patient mutations, the amino-terminal P50L XLID patient mutation neither impacts assembly nor catalytic activity of CRL4B-based E3 ligase complexes *in vitro*. Instead, we demonstrate that this mutation affects CUL4B's mitotic function by reducing mitotic T49 phosphorylation, thereby preventing its interaction with phospho-specific DCAFs such as LIS1 and WDR1. This regulatory mechanism could explain why CRL4A fails to compensate CRL4B-specific functions causing XLID. Consistent with CRL4B regulating cytoskeletal dynamics, comprehensive analysis reveals that intellectual disability genes converge onto a few biological modules, including cytoskeleton alterations that impact neuronal migration, neurogenesis, and synaptic plasticity (Liaci *et al*, 2021). Interestingly, LIS1 mutations are strongly linked to classical lissencephaly (LIS), a neuronal disorder characterized by brain malformation and intellectual disability caused by defects in neuronal migration (Wynshaw-Boris, 2007). Likewise, patients with mutations in WDR1 not only exhibit a mild form of intellectual disability but also suffer from aberrant lymphoid immunity (Pfajfer *et al*, 2018).

Human forebrain organoids allowed us to model brain development, revealing a CRL4B-specific ventricular phenotype during forebrain differentiation. The ventricular structures of forebrain organoids are the compartments for proliferation, while differentiated cells form layers around the ventricles (Di Lullo & Kriegstein, 2017). The uncovered mitotic delay and spindle positioning defect of cells lacking CUL4B function might explain the brain organoid phenotype. A similar ventricular phenotype is observed in Miller-Dieker syndrome (MDS), which is caused by loss of LIS1. Indeed, MDS organoids exhibit impaired spindle positioning and a partial loss of the inner ventricular structure (Iefremova *et al*, 2017), which resembles the observed loss of ventricles in ΔCUL4B organoids. In addition, live-cell imaging of heterozygous LIS1+/− organoids reveals, apart from spindle positioning defects, a prolonged mitosis, accompanied by changes in the expression of cytoskeletal and extra-cellular matrix proteins (Karzbrun *et al*, 2018). In light of these findings, and the fact that CRL4B mutations correlate with XLID and related intellectual disability disorders, we speculate that an unconventional $pCRL4B^{LIS1}$ E3-ligase regulates mitosis and spindle positioning during brain development.

Materials and Methods

Antibodies and reagents

For western blot and immunofluorescence analysis, following primary antibodies were used: Anti-Actin (mouse, Merck Millipore); Anti-ARP3 (mouse, Santa Cruz); Anti-CK1α (mouse, Santa Cruz); Anti-CUL4A (rabbit); Anti-CUL4-CT (rabbit) (Olma *et al*, 2009); Anti-CUL4B (rabbit, Sigma); Anti-DCTN1 (rabbit, Atlas antibodies); Anti-DDB1 (mouse, BD Biosciences); Anti-GAPDH (mouse, Sigma); Anti-HA.II (mouse or rabbit, both Covance); Anti-Histone 4 (rabbit, Abcam); Anti-Phospho-Histone H2A.X S139 (mouse, Merck Millipore); Anti-Phospho-Histone H3 S10 (rabbit, Upstate); Anti-LIS1 (mouse, Santa Cruz Biotechnology); Anti-Pericentrin (rabbit, Covance); Anti-Tubulin (mouse, Sigma); Anti-WDR1 (rabbit, Atlas antibodies); Anti-SOX2 (rabbit, Millipore, AB5603); Anti-CTIP (rat, Abcam, ab18465); Anti-β-catenin (mouse, Millipore, AB5733); and Anti-Ki67 (rat, eBioscience, 14-5698-82). For western blot Anti-mouse or rabbit IgG-HRP (both Bio-rad) and for immunofluorescence anti-mouse or rabbit IgG-Alexa 488, 568, and 647 (Invitrogen), secondary antibodies were used. Rhodamine phalloidin dye was used for acting staining.

Cell culture, RNAi, and transient transfection

Cells were cultured at 37°C with 5% CO_2 in DMEM (Gibco) supplemented with 10% FCS and 1% penicillin–streptomycin-glutamine (Gibco). RNAi experiments were performed according to the manufacturer's instructions with 25 nM double-stranded siRNA and Lipofectamine RNAiMax (Invitrogen). Depending on the experiments, the cells were harvested 48 to 96 h after RNAi. siRNAs (Microsynth) used: siCUL4A (5′-GAATCCTACTGTTGATCGATT), siCUL4B (5′-AGCGCCTGTTAGTCGGAAA), siDDB1 (5′-ACTAGATCGCGATAAATT), siLIS1 (5′-CGGACAAGTAGAATAAATGTT), siWDR1 (5′-GGTGGGATTTAGGCAATTATT), and AllStars Negative Control siRNA (Qiagen).

Transient transfection was accomplished using lipofectamine 3000 (Invitrogen) and FLAG-CUL4B and mutants in pcDNA5/FRT/TO vector (Invitrogen).

Generation of stable cell lines

The CUL4B knockout cell lines were achieved with SpCas9-mediated genome editing based on the protocol of Ran *et al* (2013b) and Ran *et al* (2013a). The gRNAs targeting the intron between exons 2 and 3 (target DNA: 5′TCCCGCGGGACCGTTAAGGA) and between exons 4 and 5 (target DNA: 5′TAACGGCTACCTATATGGTA) were cloned into a pX458 plasmid, kindly provided by F. Zhang (Addgene plasmid #48138; Ran *et al*, 2013b) and were transient transfected using lipofectamine 3000 transfection reagent (Invitrogen). GFP-positive cell sorting in a BD FACSAria IIIu cell sorter (BD Biosciences) was performed 4 days after transfection. Individual clones were picked and tested for CUL4B deletion by western blot. Knock-in of HA-tagged CUL4B or mutants in the CUL4B gene locus was achieved by targeting two regions within exon 3 (target DNA 1: GGTGCTGGTATTACCATCAG; target DNA 2: ACTAACTTCTTAGCAGAGCC). The pX458 plasmids containing the gRNAs were co-transfected with pUC18 plasmid, the Puro-P2A-HA containing template vector for homologous recombination. Four days after transfection, cells were selected with 1 μg/ml puromycin. Individual clones were picked and tested by western blot.

Generation of Flp-In T-Rex HeLa cell ($HeLa_{FLP}$) lines with inducible expression of CUL4B or mutants was accomplished with co-transfection of pcDNA5-pDEST-FRT-CUL4B/ mutants and the pOG44 vectors adapted from Kean *et al* (2012). Cells were selected 24 h after transfection with 200 μg/ml Hygromycin B, and single colonies were picked and tested for Doxycycline-inducible expression of CUL4B and mutants.

MTT assay

Twenty-four hours after RNAi 2.5×10^3 cells per well were seeded in 4 × 96-well plates with three technical replicates per condition. The MTT assay kit (Promega) was used according to the manufacturer's instructions. The MTT dye master mix was incubated for 2 h at 37°C and 5% CO_2 on the cells, and the reaction was stopped with

the addition of 100 µl stop solution. The plate was measured at a wavelength of 570 nm, and the growth rate was calculated normalizing to day 0.

SDS–PAGE and Western blot

Samples were either run on 4–12% NuPAGE or Bolt gels with the NuPAGE Bis–Tris system (Invitrogen) in MOPS SDS buffer or on 8% gels with the Bio-Rad system with SDS-running buffer. Western blotting was performed with the wet transfer systems from Bio-Rad on 0.45 µm Nitrocellulose membranes (Amersham™), which were blocked in 5% milk in PBS. Primary antibody dilutions were 1:500 in 5% milk-PBS, while secondary antibodies were diluted 1:2,000. Blots were visualized with SuperSignal™ West Pico PLUS or Femto Chemiluminescent Substrate solution (Thermo Fischer) or with Clarity™ Western ECL solution (Bio-Rad) and scanned on Fusion FX7 imaging system (Witec AG).

Flow cytometry

Cells were harvested with 0.5% Trypsin solution (Thermo Fischer), washed with PBS after centrifugation at 500 *g* for 5 min, and then resuspended in 70% ethanol solution precooled to −20°C. After an incubation at −20°C for at least 2 h, cells were centrifuged, washed 2× with PBS supplemented with 0.05% Triton X-100 (Sigma), and resuspended in blocking buffer (PBS, 0.25% Triton X-100, 5% FCS) for 30 min. Cells were incubated for 1 h in blocking buffer supplemented with the indicated antibody, washed 2× with washing buffer (PBS, 0.1% Triton X-100, 5% FCS), and incubated for 1 h in blocking buffer supplemented with the appropriate secondary anti-IgG antibody, conjugated to Alexa 488. Following 2× washes with washing buffer, cells were resuspended in PBS supplemented with 50 µg/ml propidium iodide (PI; Sigma) and 20 µg/ml RNAse A (Thermo Fischer). Flow cytometry was carried out in a FACSCalibur instrument (BD Biosciences). If no antibody staining was performed, blocking and antibody incubation steps were omitted.

Immunofluorescence

Cells were seeded on coverslips 1 or 2 days before fixation with 4% PFA for 10 min. For cytoplasmic pre-extraction, cells were incubated with extraction buffer (20 mM PIPES pH 6.8, 10 mM EGTA, 1 mM $MgCl_2$ and 0.25% Triton X-100) for 4 min before fixation. Cells were permeabilizated with 0.25% Triton X-100 in PBS and washed with PBS with 0.05% Triton X-100. Blocking buffer (PBS, 0.05% Triton X-100, 5% FCS) was used for 30 min before the primary antibody dilution 1:500, which was incubated for 1 h at RT. The samples were washed three times and incubated for 1 h with 1:4,000 secondary anti-mouse IgG and anti-rabbit IgG antibodies, conjugated to Alexa 488, Alexa 568, or Alexa 647. After three washes, the coverslips were mounted on, slides with Immu-mount (Thermo Scientific). The second wash was supplemented with 0.1 µg/ml DAPI (Sigma) and for cytoskeletal staining phalloidin dye. For DNA damage assessment, cells were imaged in a single plan with a 20× objective, while for chromatin exclusion and spindle positioning Z-stacks of cells were acquired in 0.33 µm steps from 5 µm to −5 µm in an Eclipse Ti epifluorescence microscope (Nikon) using a 60× oil objective (NA 1.4 Plan Apochromat). Example images for spindle positioning were taken with the Olympus Fluoview 3000. Image analysis was performed with ImageJ converting Z-stacks to maximum projections using the same contrast settings of per channel for all the conditions. Nuclear intensity was measured with a mask based on DAPI signal, while spindle positioning was measured based on the pericentrin signal localization in regard to the center of the cells.

Live-cell imaging

For mitotic duration assessment, around 10,000 cells were reseeded in 8-well µ-Slide chambers (Ibidi) after 48 h of siRNA treatment or 24 h of Doxycycline induction in 6-well plates. Cells were imaged every 3 min in the bright-field channel (BF) on the Eclipse Ti epifluorescence microscope (Nikon Instruments), at 37°C and 5% CO_2 and stable humidity, using a 10× objective (NA 0.45 CFI Plan Apochromat). For mitotic duration, approximately 10 cells per movie were analyzed counting the frames from rounding of the cell to cytokinesis of a single cell. The spindle movement was assessed with the HeLa Kyoto H2B-mcherry and lifeAct-GFP cells, which were a kind gift from B. Baum (Matthews *et al*, 2012). Imaging was performed as described above every 3 min in BF, RFP, and GFP channels with 5% LED intensity. To track the position of the mitotic plate, an in-house IGOR (WaveMatrics) code was used. Only cells that both entered and completed mitosis during each time-lapse recording were analyzed. In each image, the spindle was found using a threshold of which the position and angle were determined by fitting an ellipse.

Cell cycle arrests

Cell cycle arrests were performed with different drugs dependent on cell cycle phase. Cells were arrested in S-phase with 2 mM thymidine (Sigma), in G2 with 10 µM RO3306 (Calbiochem) and in mitosis with 100 ng/µl nocodazole (Sigma) or taxol (Paclitaxel, Sigma) for 24 h. Mitotic arrest for AFM experiments was performed with 2 µM (+)-*S*-trityl-L-cysteine (STC, Sigma) for 1 h.

G2 block and release

Cells were seeded in 6-well plates and arrested in G2 for 20 h with 10 µM RO3306 (Calbiochem) addition. Release was performed with 2× PBS washes and 1 media wash. Synchronized cells were harvested at different time points after the release in 1× Laemmli buffer.

λ-Phosphatase treatment

Around 4×10^6 cells were lysed in 1× PMP buffer supplemented with 1 mM $MnCl_2$, 0.5% NP40, 0.5 mM PMSF, and protease inhibitor cocktail. Lysates were split in two tubes and either 200 U λ-Phosphatase or lysis buffer were added, followed by an incubation for 1 h at 30°C.

Protein expression and purification

cDNAs encoding human CUL4B (Q13620), DDB1 (Q16531), WDR1 (O75083), and LIS1 (P43034) were cloned into pAC8 vector, which is derived from the pBacPAK8 system (ClonTech). CUL4A (FL)

(Q13619) and DDB1 (FL) (Q16531) were assembled into the same vector (pBIG1a) using Gibson-based technique (biGBac) (Weissmann *et al*, 2016; Mohamed *et al*, 2021). FLAG-tagged CUL4, DDB1, or RBX1 constructs were also cloned into pFL multiBac vectors. Bacmids were produced in DH10Bac/Multibac E. coli bacterial strains and extracted as previously described (Fitzgerald *et al*, 2006). Recombinant baculoviruses were prepared in *Spodoptera frugiperda* (*Sf9*) cells using Cellfectin (Invitrogen) following the Bac-to-Bac protocol (Life Technologies). Recombinant protein complexes were expressed in *Sf9* or *Trichoplusia ni* High Five cells by co-infection of single baculoviruses. For the CRL4B WT or NP1 complexes (CUL4B, DDB1, and Rbx1), the CUL4B (WT or NP1 mutant) was expressed with N-terminal Strep (II) tag and DDB1 and RBX1 with N-terminal His-tag. For the CRL4A complex (CUL4A, DDB1, and Rbx1), all components were expressed with an N-terminal His-tag. WDR1 (FL) or (ΔN; 29–606) and LIS1 (FL) or (ΔN; 99–410) were expressed separately, each with an N-terminal Strep (II) tag, or Strep II-Avi tag. Cells were harvested 48 h after infection and lysed by sonication in a buffer containing Tris–HCl pH 8.0, 200 mM NaCl, and 0.5 mM TCEP, including 0.1% Triton X-100, 1× protease inhibitor cocktail (Roche Applied Science), and 1 mM phenylmethanesulfonyl fluoride (PMSF). Lysates were cleared by ultracentrifugation for 45 min at 40,000 *g*. The supernatant was loaded on Strep-Tactin (IBA life sciences) or Ni-NTA (Sigma) affinity chromatography resins in a buffer containing Tris–HCl pH 7.5, 200 mM NaCl and 0.5 mM TCEP. The Strep (II) and Ni-NTA elution fractions were further purified via ion exchange chromatography (Poros HQ 50 μm, Life Technologies) and subjected to size-exclusion chromatography in a buffer containing 50 mM HEPES pH 7.4, 200 mM NaCl, 0.5 mM TCEP, and 10% glycerol. Pure fractions, as judged by SDS–PAGE, were collected and concentrated using 10,000 MWT cutoff centrifugal devices (Amicon Ultra) and stored at −80°C. For FLAG-tagged CUL4A/B, DDB1, RBX1 complex, infected cells were resuspended lysed in buffer containing 50 mM Tris–HCl pH 8.0, 350 mM NaCl, 0.4% Triton X-100, 1 mM EDTA, 1 mM DTT, and protease inhibitor cocktail (Roche), using a Dounce homogenizer. Lysates were cleared by centrifugation at 12,000 *g* for 30 min at 4°C and loaded into anti-FLAG M2 affinity gel (Sigma). Washes were performed in buffer containing 50 mM Tris–HCl pH 8.0 and 150 mM NaCl, and CRL4 complexes were subsequently eluted with 3×FLAG peptide diluted in 50 mM Tris–HCl pH 8.0, 150 mM NaCl and 10% glycerol, frozen in liquid nitrogen and stored at −80°C until analysis.

In vitro kinase assay

Around 0.5 μg of recombinant FLAG-CUL4A or FLAG-CUL4B (in complex with DDB1 and RBX1) or 0.15 μg native swine myelin basic protein (MBP; SignalChem) were added to 1× protein kinase buffer (NEB) supplemented with 200 μM "cold" ATP (Sigma) and 500 μCi/μmol ATPγ^{32}P (Hartmann Analytic). The reaction was initiated by the addition of 10 U (pmol/min) of recombinant CK1 (NEB), CDK1-cyclin B1 (NEB), PLK1 (SignalChem), Aurora A (SignalChem) or Aurora B (SignalChem) kinases, incubated for 1 h at 30°C. Samples were boiled in 1× Laemmli buffer and subjected to SDS–PAGE. Gels were stained with InstantBlue Coomassie stain (Expedeon Protein Solutions), vacuum-dried for 30 min, and exposed overnight to a storage phosphor screen (GE Healthcare). Screens were scanned in a Typhoon FLA 9000 system (GE Healthcare).

In vitro ubiquitination assay

CRL4B^{CRBN} complexes were assembled by mixing CRL4B WT, NP1, or P50L mutants at 117.5 nM with 12.5 nM DDB1-CRBN in the presence of 10 μM Lenalidomide. *In vitro* ubiquitination of the substrate CK1α was performed by mixing the assembled CRL4B^{CRBN} complexes with a reaction mixture containing UBE1 at 1 μM, UBCH5a at 0.5 μM, Ubiquitin at 15 μM, and 0.25 μM CK1α, as indicated. Reactions were carried out in 50 mM Tris–HCl pH 7.6, 3 mM ATP, 0.5 mM DTT, and 10 mM $MgCl_2$ and incubated for 0–10 min at 37 °C.

In vitro pull-down assays

For pull-down assays in *Sf9 cells*, 150 μl of baculoviruses of His-DDB1 and FLAG-WDR1 or LIS1, or Strep-DCAF8 and Strep-CUL4B were co-infected in 10 ml of *Sf9* cells. Infected cells were incubated at 27 °C for 48 h and lysed by sonication in a buffer containing Tris–HCl pH 8, 200 mM NaCl and 0.5 mM TCEP, including 0.1% Triton X-100, 1× protease inhibitor cocktail (Roche Applied Science), 1 mM PMSF, and 10% glycerol. Lysates were cleared by centrifugation at 14,000 *g* for 30 min, and 1 ml of soluble protein fractions was incubated for 1 h at 4°C with 20–30 μl Strep-Tactin Macroprep beads (IBA Lifesciences), FLAG or Ni-NTA beads (Sigma). Beads were washed three times with lysis buffer, and bound proteins were eluted in 20–30 μl of SDS loading dye and heated at 95°C for 2 min.

For pull-down assays using purified protein complexes, Strep-tag was cut out of the CRL4B WT and mutant, and CRL4A complexes by the His-tagged TEV-protease. TEV was then removed by loading the cleaved sample on Ni-NTA beads (Sigma). CDK1 phosphorylation was performed at 30°C for 2.5 h in 1× PK buffer, ATP (2 mM), CRL4B (14 μM), and 19.8 μl CDK1-cyclin B (20,000 U/ml). Dephosphorylation of CRL4B took place in a 100 μl reaction mixture containing 86 μl of CRL4B protein (at 0.8 mg/ml) with 2 μl λ-phosphatase (λ-PP) in the presence of 0.1 mM $MnCl_2$ and 1× PMP reaction buffer (NEB). Untagged-CRL4 complexes (4A, 4B WT, 4B NP1, and λ-PP-treated 4B) were incubated with Strep-tagged LIS1 or WDR1 at 1:1 molar ratio of 1.5 μM in 35 μl. Reaction mixture was loaded on 5 μl Strep-resin (IBA bioscience) and shaking at room temperature. Beads were washed four times with 500 μl of buffer containing HEPES pH 7.2 50 mM, NaCl 200 mM, and TCEP 0.5 mM, followed by the addition of 15 μl SDS loading dye on the washed beads before loading 10 μl on NuPAGE (Thermo Fischer). Quantification of band intensities was carried out in ImageJ. CUL4 band intensities were normalized to the band intensity of LIS1 or WDR1.

Biotinylation

Purified StrepII-Avi-tagged LIS1 or pII-Avi-tagged WDR1 was biotinylated *in vitro* at a concentration of 50 and 38 μM, respectively. Reaction was incubated with 2.5 μM BirA enzyme and 0.2 mM D-Biotin in 50 mM HEPES pH 7.4, 200 mM NaCl, 10 mM MgCl2, 0.5 mM TCEP, and 20 mM ATP. The reaction was incubated for 3 h at room temperature and at 4 °C overnight. Biotinylated proteins were purified by size-exclusion chromatography and stored at −80°C.

Fluorescence polarization

Alexa488-coupled streptavidin (Thermo Fischer) was incubated at 20 μM in 1:1 molar ratio with biotinylated LIS1 (20 μM) or WDR1 (18 μM) for 30–60 min at room temperature, and buffer exchange (Zeba Spin) was performed in the reaction buffer (HEPES pH 7.4, NaCl 200 mM, D-Trehalose 25 mM, Triton X-100 0.01%, TCEP 0.5 mM, and BSA 0.1 mg/ml). Twenty-six nM of Alexa-labeled LIS1 or 15 nM WDR1 was titrated with increasing concentrations of DDB1, CRL4B, or CRL4A as indicated. Reactions took place at room temperature in 384-well plates in a BMG Clariostar plate reader (BMG LabTech). Binding affinities were calculated by measuring the change in fluorescence polarization. Data were plotted and analyzed using GraphPad Prism assuming a single site binding saturation.

Cell fractionation

The NE-PER Nuclear and Cytoplasmic Extraction Reagents (Thermo Fischer) were used according to the manufacturer's instructions to isolate the nuclei. Forty-eight hour after transfection, around 4 million cells were harvested by trypsinization and nuclei were isolated and cytoplasmic samples were taken. The isolated nuclei were lysed in a buffer containing 10 mM Hepes-KOH pH 7.7, 100 mM KCl, 50 μM sucrose, 0.25% Triton X-100, and protease inhibitor cocktail with a 27G syringe. Nuclear lysates were then loaded on top of a 1 M sucrose cushion and centrifuged at 8,000 *g* for 30 min. To separate the pellet (DNA bound) and the soluble fraction, the lysates were loaded on a 1 M sucrose cushion and centrifuged for 30 min at 8,000 *g*. Samples were boiled in 1× Laemmli buffer for 5 min at 95°C followed by SDS–PAGE and western blot.

Immunoprecipitation

Around 4×10^7 cells expressing HA-CUL4B or mutants were harvested in a NEDD8 block (Reichermeier *et al*, 2020). Thus, 1 μM MLN4924 and CSN5i-3 was added to the PBS wash and to the lysis buffer (IP buffer plus DTT). Lysis was performed for 40 min using a 27G needle syringe and with the addition of 125 U pierce universal nuclease (Thermo Fischer). The IP buffer contained 20 mM HEPES pH 7.9, 100 mM KCl, 2 mM $MgCl_2$, 0.5% NP40, 300 mM sucrose, 10 mM NaF, 10 mM β-glycerophosphate, 0.2 mM $NaVO_4$, and 1 mM PMSF. After centrifugation for 30 min at 16,000 *g*, protein concentration was measured with Quick Start Bradford reagent (Bio-Rad) and normalized to lowest sample. Samples were incubated with anti-HA-agarose beads (Sigma; clone HA-7) for 1 h at 4°C. The beads were washed 5× with IP buffer. Proteins were eluted with 1× Laemmli buffer and analyzed on SDS–PAGE followed by western blot.

Profiling of CUL4B phosphorylation sites by quantitative mass spectrometry

HA-tagged CUL4B was immunoprecipitated from around 1×10^8 mitotic cells as described above. After a last wash with MilliQ water, the dried beads were frozen in liquid nitrogen and stored at −80°C. The proteins were eluted from beads by 3 × 30 min incubation in 6 M urea/2 M thiourea at room temperature. Supernatants were reduced with 1 mM DTT and alkylated with 5.5 mM chloroacetamide. Proteins were predigested with 1:100 w/w LysC (Wako) for 4 h, diluted in 4 volumes of water, and digested with 1:100 w/w trypsin (Serva) overnight. Samples were incubated in TFA (0.5% V/V) for 1 h at 4°C and centrifuged for 10 min at 4,000 *g*. Peptide supernatants were purified using C18 Sep-Pak columns (Waters), eluted in 50% acetonitrile, and acidified with TFA to 6% V/V. Phosphopeptides were enriched using titanium dioxide resin as described (Borisova *et al*, 2017) and desalted using reversed-phase C18 StageTips (Rappsilber *et al*, 2007).

Samples were analyzed on a quadrupole Orbitrap mass spectrometer (Exploris 480, Thermo Scientific) equipped with a UHPLC system (EASY-nLC 1,200, Thermo Scientific). They were loaded onto a C18 reversed-phase column (55 cm length, 75 mm inner diameter) and eluted with a gradient from 2.4 to 32% ACN containing 0.1% formic acid in 90 min. The mass spectrometer was operated in data-dependent mode, automatically switching between MS and MS2 acquisition. Survey full-scan MS spectra (m/z 300–1,650, resolution: 60,000, target value: 3e6, maximum injection time: 60 ms) were acquired in the Orbitrap. The 15 most intense precursor ions were sequentially isolated, fragmented by higher energy C-trap dissociation (HCD), and scanned in the Orbitrap mass analyzer (normalized collision energy: 30%, resolution: 30,000, target value: 1e5, maximum injection time: 60 ms, isolation window: 1.4 m/z). Precursor ions with unassigned charge states, as well as with charge states of +1 or higher than +6, were excluded from fragmentation. Precursor ions already selected for fragmentation were dynamically excluded for 25 s. Raw data files were analyzed using MaxQuant (version 1.5.2.8; Cox & Mann, 2008). Site localization probabilities were determined by MaxQuant using the post-translational modification scoring algorithm. Parent ion and MS2 spectra were searched against a reference proteome database containing human protein sequences obtained from UniProtKB (version 2020_02) using Andromeda search engine (Cox *et al*, 2011). Spectra were searched with a mass tolerance of 6 p.p.m. in MS mode, 20 p.p.m. in HCD MS2 mode, strict trypsin specificity, and allowing up to two miscleavages. Cysteine carbamidomethylation was searched as a fixed modification, whereas protein N-terminal acetylation, methionine oxidation, phosphorylation (STY), and N-ethylmaleimide modification of cysteines (mass difference to cysteine carbamidomethylation) were searched as variable modifications. The dataset was filtered based on posterior error probability (PEP) to arrive at a false discovery rate of below 1% estimated using a target-decoy approach (Elias & Gygi, 2007).

CUL4B interaction profiling by quantitative mass spectrometry

HA-tagged CUL4B or the phosphorylation-deficient mutants NP1 and P50L were immunoprecipitated as described above from around 7.5×10^7 SILAC-labeled and nocodazole-arrested cells (mitotic). During the last wash, the beads from all three conditions were combined. Bound proteins were eluted in 2× NuPAGE LDS Sample Buffer (Life Technologies) supplemented with 1 mM DTT, heated at 70 °C for 10 min, alkylated by the addition of 5.5 mM chloroacetamide for 30 min, and separated by SDS–PAGE on a 4–12% gradient Bis–Tris gel. Proteins were stained using the Colloidal Blue Staining Kit (Life Technologies) and digested in-gel using trypsin (Serva). Peptides were extracted from the gel using a series of increasing

acetonitrile percentages and desalted using reversed-phase C18 StageTips. MS acquisition and analysis were performed as described above with the following modifications. Peptide fractions were analyzed on a quadrupole Orbitrap mass spectrometer (Q Exactive Plus, Thermo Scientific) equipped with a UHPLC system (EASY-nLC 1000, Thermo Scientific). Peptide samples were loaded onto C18 reversed-phase columns (23 cm length, 75 µm inner diameter, and 1.9 µm bead size) and eluted with a linear gradient from 1.6 to 52% acetonitrile containing 0.1% formic acid in 175 min. The mass spectrometer was operated in a data-dependent mode, automatically switching between MS and MS2 acquisition. Survey full-scan MS spectra (m/z 300–1,650, resolution: 70,000, target value: 3e6, maximum injection time: 20 ms) were acquired in the Orbitrap. The 10 most intense ions were sequentially isolated, fragmented by higher energy C-trap dissociation (HCD), and scanned in the Orbitrap mass analyzer (resolution: 35,000, target value: 1e5, maximum injection time: 120 ms, isolation window: 2.6 m/z). Precursor ions with unassigned charge states, as well as with charge states of +1 or higher than +7, were excluded from fragmentation. Precursor ions already selected for fragmentation were dynamically excluded for 25 s. MaxQuant analysis was performed as described above, without setting phosphorylation (STY) as a variable modification. Potential contaminants, reverse hits, hits only identified by site, and hits with no unique peptides were excluded from the analysis.

Atomic force microscopy

Experiments were performed using an AFM setup (CellHesion 200; JPK Instruments) mounted on an inverted microscope (Observer Z1; Carl Zeiss Microscopy). Optical images were recorded with a Plan-Apochromat (25×/0.8NA) water immersion objective. AFM cantilevers with nominal spring constants of 150 mN/m and 350 µm in length (NSC12/tipless/No A1/MikroMasch) were modified with polydimethylsilane (PDMS; Sylgrad 184; Dow Corning) wedges to correct for tilt angle of the cantilever (Stewart *et al*, 2013). The spring constant of wedged cantilevers was determined using the thermal noise method (Hutter & Bechhoefer, 1993). Cells were seeded and grown overnight in cover glass bottom dishes (WPI). Two µM (+)-S-trityl-l-cysteine (STC, Sigma Aldrich) was added 30 min before starting measurements. For each confinement measurement, an isolated mitotic cell was identified and DIC imaged before, during, and after confinement by the wedged AFM cantilever. Optical images were used to determine cell diameter. The wedged end of the cantilever was lowered onto the glass bottom in the vicinity of the cell. Using a programmed procedure, the end was first raised 30 µm at 5 µm/s, held at this height for 20 s while the end of the cantilever was manually positioned above the cell, and lowered 22 µm at 1 µm/s to confine the cell. The height of the cantilever was maintained for 60s of confinement, before the cantilever was raised 22 µm at 1 µm/s and the end was repositioned above the glass bottom and finally lowered on to the glass at 5 µm/s. Cantilever height and the force acting on the cantilever were recorded at 100 Hz, and the data were processed using JPK analysis software and IGOR (WaveMatrics). Cell diameters were determined using Axiovision (Zeiss) or ImageJ. Cortex tension was determined using a fluid-filled model of rounded mitotic cells (Fischer-Friedrich *et al*, 2014).

Human embryonic stem cell handling

All H9 hESC experiments were approved by the Kantonale Ethik-Kommission (KEK) of the Canton of Zurich, Switzerland. H9 hESCs were stored, maintained, and passaged as previously described (Denoth-Lippuner *et al*, 2021). The cell division history of individual cells in complex tissues was visualized using iCOUNT. To knockout CUL4B, approximately 2 million H9 hESCs were electroporated with 4 µg of each CRISPR/cas9 expressing plasmid using an AMAXA electroporation system (Lonza). 24-h postelectroporation, H9 hESCs were passaged and single cells were sorted into individual wells of 96-well plates. After clonal colony expansion, a portion of each single cell colony was lysed and deletion of CUL4B was verified by western blotting.

Human forebrain organoid development and quantification of cortical units

H9 hESCs were used as starting population to generate human forebrain-specific regionalized organoids as described previously (Denoth-Lippuner *et al*, 2021). Twenty µm organoid sections were stained with the indicated antibodies. All images were analyzed using ImageJ, and the data were processed using Excel or Prism. The DAPI channel was used to determine the organoid area. Cortical units were quantified manually, by defining the dense ring of SOX2-positive nuclei, orientated toward the center of the ring, and surrounded by CTIP2-positive nuclei. Proliferation analysis was performed by counting the number of Ki67 and SOX2-positive nuclei in relation to the number of SOX2-positive nuclei. Ventricles were defined as beta-catenin-positive regions, largely devoid of DAPI-positive nuclei, and surrounded by SOX2-positive nuclei orientated inwards. Ventricles were counted and the number divided by the total organoid area.

Data presentation and statistical analysis

Statistical analysis and visualization of MS data were performed using the R software environment (version 4.2.1). GO terms analysis was performed on CUL4B interactors with at least twofold enrichment in interaction with WT versus NP1 mutant using the R package ViseaGO (Brionne *et al*, 2019) with full human UniProt proteome used as a background. Quantification of images and movies was performed with ImageJ or IGOR (WaveMatrics), which was also used for the analysis of the AFM data. GraphPad Prism was used to generate graphs and perform statistical analysis. For experiments comparing to conditions, *t*-tests were performed, while for multiple conditions 1-ANOVA was used followed by Dunnett's multiple comparisons test.

Data availability

The mass spectrometry-based proteomics data have been deposited to the ProteomeXchange Consortium via the PRIDE partner repository with the dataset identifier PXD035329 (https://www.ebi.ac.uk/pride/archive/projects/PXD035329).

Expanded View for this article is available online.

Acknowledgments

We would like to thank B. Baum for kindly providing the HeLa Kyoto H2B-mcherry and lifeAct-GFP cells. We thank ScopeM and especially S.-S. Lee for microscopy training and support, R. Prashant and F. Lampert for help with cell culture experiments and CRL4B^{CRBN} ubiquitination assays, and J. Chen and the Proteomics Core Facility at IMB Mainz for assisting the mass spectrometry analysis. We thank K. Reichermeier and D. Kirkpatrick, as well as R. Aebersold for initial mass spectrometry experiments and advice. We are grateful to U. Kutay, P. Meraldi, N. Thomä and members of the Peter laboratory for helpful discussions, and A. Smith for critical editing. Work in the Peter laboratory is supported by the Swiss National Science Foundation (310030_179283/1), the Swiss Cancer league (Krebsliga Schweiz) and ETH Zürich. Work in the Beli laboratory is funded by the Deutsche Forschungsgemeinschaft (DFG, German Research Foundation)—Project-ID BE 5342/2-1—FOR 2800. Open access funding is provided by ETH Zurich. L.N.R. was supported by the Boehringer Ingelheim Fonds. Open access funding provided by Eidgenossische Technische Hochschule Zurich.

Author contributions

Anna Stier: Conceptualization; data curation; formal analysis; investigation; methodology; writing – original draft; writing – review and editing. **Samuel Gilberto:** Conceptualization; data curation; formal analysis; investigation; methodology; writing – original draft; writing – review and editing. **Weaam I Mohamed:** Conceptualization; data curation; investigation; methodology; writing – original draft; writing – review and editing. **Lars N Royall:** Conceptualization; data curation; formal analysis; writing – review and editing. **Jonne Helenius:** Formal analysis; investigation; methodology. **Ivan Mikicic:** Formal analysis; investigation; methodology; writing – review and editing. **Tatjana Sajic:** Formal analysis; methodology. **Petra Beli:** Conceptualization. **Daniel J Müller:** Conceptualization. **Sebastian Jessberger:** Conceptualization. **Matthias Peter:** Conceptualization; supervision; funding acquisition; writing – original draft; project administration; writing – review and editing.

Disclosure and competing interests statement

The authors declare no conflict of interest. Matthias Peter is a member of the Advisory Editorial Board of *The EMBO Journal*. This has no bearing on the editorial consideration of this article for publication.

References

Alexander J, Lim D, Joughin BA, Hegemann B, Hutchins JR, Ehrenberger T, Ivins F, Sessa F, Hudecz O, Nigg EA *et al* (2011) Spatial exclusivity combined with positive and negative selection of phosphorylation motifs is the basis for context-dependent mitotic signaling. *Sci Signal* 4: ra42

Borisova ME, Wagner SA, Beli P (2017) Mass spectrometry-based proteomics for quantifying DNA damage-induced phosphorylation. *Methods Mol Biol* 1599: 215 – 227

Bowes C, Redd M, Yousfi M, Tauzin M, Murayama E, Herbomel P (2019) Coronin 1A depletion restores the nuclear stability and viability of Aip1/Wdr1-deficient neutrophils. *J Cell Biol* 218: 3258 – 3271

Brionne A, Juanchich A, Hennequet-Antier C (2019) ViSEAGO: a Bioconductor package for clustering biological functions using gene ontology and semantic similarity. *BioData Mining* 12: 16

Cabezas DA, Slaugh R, Abidi F, Arena JF, Stevenson RE, Schwartz CE, Lubs HA (2000) A new X linked mental retardation (XLMR) syndrome with short stature, small testes, muscle wasting, and tremor localises to Xq24-q25. *J Med Genet* 37: 663 – 668

Chaikovsky AC, Li C, Jeng EE, Loebell S, Lee MC, Murray CW, Cheng R, Demeter J, Swaney DL, Chen SH *et al* (2021) The AMBRA1 E3 ligase adaptor regulates the stability of cyclin D. *Nature* 592: 794 – 798

Chen CY, Tsai MS, Lin CY, Yu IS, Chen YT, Lin SR, Juan LW, Chen YT, Hsu HM, Lee LJ *et al* (2012) Rescue of the genetically engineered Cul4b mutant mouse as a potential model for human X-linked mental retardation. *Hum Mol Genet* 21: 4270 – 4285

Cox J, Mann M (2008) MaxQuant enables high peptide identification rates, individualized p.p.b.-range mass accuracies and proteome-wide protein quantification. *Nat Biotechnol* 26: 1367 – 1372

Cox J, Neuhauser N, Michalski A, Scheltema RA, Olsen JV, Mann M (2011) Andromeda: a peptide search engine integrated into the MaxQuant environment. *J Proteome Res* 10: 1794 – 1805

Dai Q, Wang H (2006) Cullin 4 makes its mark on chromatin. *Cell Div* 1: 14

Denoth-Lippuner A, Jaeger BN, Liang T, Royall LN, Chie SE, Buthey K, Machado D, Korobeynyk VI, Kruse M, Munz CM *et al* (2021) Visualization of individual cell division history in complex tissues using iCOUNT. *Cell Stem Cell* 28: 2020 – 2034.e12

Deshaies RJ, Emberley ED, Saha A (2010) Control of cullin-ring ubiquitin ligase activity by nedd8. *Subcell Biochem* 54: 41 – 56

Di Lullo E, Kriegstein AR (2017) The use of brain organoids to investigate neural development and disease. *Nat Rev Neurosci* 18: 573 – 584

Elia AE, Cantley LC, Yaffe MB (2003) Proteomic screen finds pSer/pThr-binding domain localizing Plk1 to mitotic substrates. *Science* 299: 1228 – 1231

Elias JE, Gygi SP (2007) Target-decoy search strategy for increased confidence in large-scale protein identifications by mass spectrometry. *Nat Methods* 4: 207 – 214

Elshenawy MM, Kusakci E, Volz S, Baumbach J, Bullock SL, Yildiz A (2020) Lis1 activates dynein motility by modulating its pairing with dynactin. *Nat Cell Biol* 22: 570 – 578

Errico A, Deshmukh K, Tanaka Y, Pozniakovsky A, Hunt T (2010) Identification of substrates for cyclin dependent kinases. *Adv Enzyme Regul* 50: 375 – 399

Fischer ES, Scrima A, Bohm K, Matsumoto S, Lingaraju GM, Faty M, Yasuda T, Cavadini S, Wakasugi M, Hanaoka F *et al* (2011) The molecular basis of CRL4DDB2/CSA ubiquitin ligase architecture, targeting, and activation. *Cell* 147: 1024 – 1039

Fischer ES, Bohm K, Lydeard JR, Yang H, Stadler MB, Cavadini S, Nagel J, Serluca F, Acker V, Lingaraju GM *et al* (2014) Structure of the DDB1-CRBN E3 ubiquitin ligase in complex with thalidomide. *Nature* 512: 49 – 53

Fischer-Friedrich E, Hyman AA, Julicher F, Muller DJ, Helenius J (2014) Quantification of surface tension and internal pressure generated by single mitotic cells. *Sci Rep* 4: 6213

Fitzgerald DJ, Berger P, Schaffitzel C, Yamada K, Richmond TJ, Berger I (2006) Protein complex expression by using multigene baculoviral vectors. *Nat Methods* 3: 1021 – 1032

Fujibuchi T, Abe Y, Takeuchi T, Imai Y, Kamei Y, Murase R, Ueda N, Shigemoto K, Yamamoto H, Kito K (2005) AIP1/WDR1 supports mitotic cell rounding. *Biochem Biophys Res Commun* 327: 268 – 275

Gilberto S, Peter M (2017) Dynamic ubiquitin signaling in cell cycle regulation. *J Cell Biol* 216: 2259 – 2271

Guerrero-Santoro J, Kapetanaki MG, Hsieh CL, Gorbachinsky I, Levine AS, Rapic-Otrin V (2008) The cullin 4B-based UV-damaged DNA-binding protein ligase binds to UV-damaged chromatin and ubiquitinates histone H2A. *Cancer Res* 68: 5014 – 5022

Hannah J, Zhou P (2015) Distinct and overlapping functions of the cullin E3 ligase scaffolding proteins CUL4A and CUL4B. *Gene* 573: 33 – 45

Higa LA, Wu M, Ye T, Kobayashi R, Sun H, Zhang H (2006) CUL4-DDB1 ubiquitin ligase interacts with multiple WD40-repeat proteins and regulates histone methylation. *Nat Cell Biol* 8: 1277 – 1283

Hu H, Zhou Q, Han X, Li Z (2017) CRL4WDR1 controls polo-like kinase protein abundance to promote Bilobe duplication, basal body segregation and flagellum attachment in *Trypanosoma brucei*. *PLoS Pathog* 13: e1006146

Hutter JL, Bechhoefer J (1993) Calibration of atomic-force microscope tips. *Rev Sci Instrum* 64: 1868 – 1873

Iefremova V, Manikakis G, Krefft O, Jabali A, Weynans K, Wilkens R, Marsoner F, Brandl B, Muller FJ, Koch P *et al* (2017) An organoid-based model of cortical development identifies non-cell-autonomous defects in Wnt signaling contributing to miller-Dieker syndrome. *Cell Rep* 19: 50 – 59

Jang SM, Zhang Y, Utani K, Fu H, Redon CE, Marks AB, Smith OK, Redmond CJ, Baris AM, Tulchinsky DA *et al* (2018) The replication initiation determinant protein (RepID) modulates replication by recruiting CUL4 to chromatin. *Nat Commun* 9: 2782

Jiang B, Zhao W, Yuan J, Qian Y, Sun W, Zou Y, Guo C, Chen B, Shao C, Gong Y (2012) Lack of Cul4b, an E3 ubiquitin ligase component, leads to embryonic lethality and abnormal placental development. *PLoS One* 7: e37070

Jin J, Arias EE, Chen J, Harper JW, Walter JC (2006) A family of diverse Cul4-Ddb1-interacting proteins includes Cdt2, which is required for S phase destruction of the replication factor Cdt1. *Mol Cell* 23: 709 – 721

Karzbrun E, Kshirsagar A, Cohen SR, Hanna JH, Reiner O (2018) Human brain organoids on a Chip reveal the physics of folding. *Nat Phys* 14: 515 – 522

Kean MJ, Couzens AL, Gingras AC (2012) Mass spectrometry approaches to study mammalian kinase and phosphatase associated proteins. *Methods* 57: 400 – 408

Kim JH, Lee SR, Li LH, Park HJ, Park JH, Lee KY, Kim MK, Shin BA, Choi SY (2011) High cleavage efficiency of a 2A peptide derived from porcine teschovirus-1 in human cell lines, zebrafish and mice. *PLoS One* 6: e18556

Kopanja D, Roy N, Stoyanova T, Hess RA, Bagchi S, Raychaudhuri P (2011) Cul4A is essential for spermatogenesis and male fertility. *Dev Biol* 352: 278 – 287

Lee J, Zhou P (2007) DCAFs, the missing link of the CUL4-DDB1 ubiquitin ligase. *Mol Cell* 26: 775 – 780

Li GF, Ji T, Chen J, Fu YF, Hou LD, Feng Y, Zhang TY, Song TY, Zhao J, Endo Y *et al* (2017) CRL4(DCAF8) ubiquitin ligase targets histone H3K79 and promotes H3K9 methylation in the liver. *Cell Rep* 18: 1499 – 1511

Liaci C, Camera M, Caslini G, Rando S, Contino S, Romano V, Merlo GR (2021) Neuronal cytoskeleton in intellectual disability: from systems biology and modeling to therapeutic opportunities. *Int J Mol Sci* 22: 6167

Liu HC, Enikolopov G, Chen YZ (2012a) Cul4B regulates neural progenitor cell growth. *BMC Neurosci* 13: 112

Liu L, Yin Y, Li Y, Prevedel L, Lacy EH, Ma L, Zhou P (2012b) Essential role of the CUL4B ubiquitin ligase in extra-embryonic tissue development during mouse embryogenesis. *Cell Res* 22: 1258 – 1269

Maddox AS, Burridge K (2003) RhoA is required for cortical retraction and rigidity during mitotic cell rounding. *J Cell Biol* 160: 255 – 265

Maiani E, Milletti G, Nazio F, Holdgaard SG, Bartkova J, Rizza S, Cianfanelli V, Lorente M, Simoneschi D, Di Marco M *et al* (2021) AMBRA1 regulates cyclin D to guard S-phase entry and genomic integrity. *Nature* 592: 799 – 803

Matthews HK, Delabre U, Rohn JL, Guck J, Kunda P, Baum B (2012) Changes in Ect2 localization couple Actomyosin-dependent cell shape changes to mitotic progression. *Dev Cell* 23: 371 – 383

Mohamed WI, Park SL, Rabl J, Leitner A, Boehringer D, Peter M (2021) The human GID complex engages two independent modules for substrate recruitment. *EMBO Rep* 22: e52981

Moon HM, Youn YH, Pemble H, Yingling J, Wittmann T, Wynshaw-Boris A (2014) LIS1 controls mitosis and mitotic spindle organization via the LIS1-NDEL1-dynein complex. *Hum Mol Genet* 23: 449 – 466

Mouysset J, Gilberto S, Meier MG, Lampert F, Belwal M, Meraldi P, Peter M (2015) CRL4(RBBP7) is required for efficient CENP-A deposition at centromeres. *J Cell Sci* 128: 1732 – 1745

Nishitani H, Sugimoto N, Roukos V, Nakanishi Y, Saijo M, Obuse C, Tsurimoto T, Nakayama KI, Nakayama K, Fujita M *et al* (2006) Two E3 ubiquitin ligases, SCF-Skp2 and DDB1-Cul4, target human Cdt1 for proteolysis. *EMBO J* 25: 1126 – 1136

O'Connell CB, Wang YL (2000) Mammalian spindle orientation and position respond to changes in cell shape in a dynein-dependent fashion. *Mol Biol Cell* 11: 1765 – 1774

Ohtake F, Baba A, Takada I, Okada M, Iwasaki K, Miki H, Takahashi S, Kouzmenko A, Nohara K, Chiba T *et al* (2007) Dioxin receptor is a ligand-dependent E3 ubiquitin ligase. *Nature* 446: 562 – 566

Olma MH, Roy M, Le Bihan T, Sumara I, Maerki S, Larsen B, Quadroni M, Peter M, Tyers M, Pintard L (2009) An interaction network of the mammalian COP9 signalosome identifies Dda1 as a core subunit of multiple Cul4-based E3 ligases. *J Cell Sci* 122: 1035 – 1044

Ono S (2018) Functions of Actin-interacting protein 1 (AIP1)/WD repeat protein 1 (WDR1) in Actin filament dynamics and cytoskeletal regulation. *Biochem Biophys Res Commun* 506: 315 – 322

Pettersson M, Crews CM (2019) PROteolysis TArgeting chimeras (PROTACs) – past, present and future. *Drug Discov Today Technol* 31: 15 – 27

Pfajfer L, Mair NK, Jimenez-Heredia R, Genel F, Gulez N, Ardeniz O, Hoeger B, Bal SK, Madritsch C, Kalinichenko A *et al* (2018) Mutations affecting the Actin regulator WD repeat-containing protein 1 lead to aberrant lymphoid immunity. *J Allergy Clin Immunol* 142: 1589 – 1604.e11

Pierce NW, Lee JE, Liu X, Sweredoski MJ, Graham RL, Larimore EA, Rome M, Zheng N, Clurman BE, Hess S *et al* (2013) Cand1 promotes assembly of new SCF complexes through dynamic exchange of F box proteins. *Cell* 153: 206 – 215

Quintyne NJ, Schroer TA (2002) Distinct cell cycle-dependent roles for dynactin and dynein at centrosomes. *J Cell Biol* 159: 245 – 254

Ran FA, Hsu PD, Lin CY, Gootenberg JS, Konermann S, Trevino AE, Scott DA, Inoue A, Matoba S, Zhang Y *et al* (2013a) Double nicking by RNA-guided CRISPR Cas9 for enhanced genome editing specificity. *Cell* 154: 1380 – 1389

Ran FA, Hsu PD, Wright J, Agarwala V, Scott DA, Zhang F (2013b) Genome engineering using the CRISPR-Cas9 system. *Nat Protoc* 8: 2281 – 2308

Rappsilber J, Mann M, Ishihama Y (2007) Protocol for micro-purification, enrichment, pre-fractionation and storage of peptides for proteomics using StageTips. *Nat Protoc* 2: 1896 – 1906

Reichermeier KM, Straube R, Reitsma JM, Sweredoski MJ, Rose CM, Moradian A, den Besten W, Hinkle T, Verschueren E, Petzold G *et al* (2020) PIKES analysis reveals response to degraders and key regulatory mechanisms of the CRL4 network. *Mol Cell* 77: 1092 – 1106.e9

Rizzelli F, Malabarba MG, Sigismund S, Mapelli M (2020) The crosstalk between microtubules, Actin and membranes shapes cell division. *Open Biol* 10: 190314

Simoneschi D, Rona G, Zhou N, Jeong YT, Jiang S, Milletti G, Arbini AA, O'Sullivan A, Wang AA, Nithikasem S *et al* (2021) CRL4(AMBRA1) is a master regulator of D-type cyclins. *Nature* 592: 789 – 793

Skowyra D, Craig KL, Tyers M, Elledge SJ, Harper JW (1997) F-box proteins are receptors that recruit phosphorylated substrates to the SCF ubiquitin-ligase complex. *Cell* 91: 209 – 219

Soucy TA, Smith PG, Milhollen MA, Berger AJ, Gavin JM, Adhikari S, Brownell JE, Burke KE, Cardin DP, Critchley S *et al* (2009) An inhibitor of NEDD8-activating enzyme as a new approach to treat cancer. *Nature* 458: 732 – 736

Stewart MP, Hodel AW, Spielhofer A, Cattin CJ, Muller DJ, Helenius J (2013) Wedged AFM-cantilevers for parallel plate cell mechanics. *Methods* 60: 186 – 194

Sugasawa K, Okuda Y, Saijo M, Nishi R, Matsuda N, Chu G, Mori T, Iwai S, Tanaka K, Tanaka K *et al* (2005) UV-induced ubiquitylation of XPC protein mediated by UV-DDB-ubiquitin ligase complex. *Cell* 121: 387 – 400

Tarpey PS, Raymond FL, O'Meara S, Edkins S, Teague J, Butler A, Dicks E, Stevens C, Tofts C, Avis T *et al* (2007) Mutations in CUL4B, which encodes a ubiquitin E3 ligase subunit, cause an X-linked mental retardation syndrome associated with aggressive outbursts, seizures, relative macrocephaly, central obesity, hypogonadism, pes cavus, and tremor. *Am J Hum Genet* 80: 345 – 352

Tripathi R, Kota SK, Srinivas UK (2007) Cullin4B/E3-ubiquitin ligase negatively regulates beta-catenin. *J Biosci* 32: 1133 – 1138

Vulto-van Silfhout AT, Nakagawa T, Bahi-Buisson N, Haas SA, Hu H, Bienek M, Vissers LE, Gilissen C, Tzschach A, Busche A *et al* (2015) Variants in CUL4B are associated with cerebral malformations. *Hum Mutat* 36: 106 – 117

Wang H, Zhai L, Xu J, Joo HY, Jackson S, Erdjument-Bromage H, Tempst P, Xiong Y, Zhang Y (2006) Histone H3 and H4 ubiquitylation by the CUL4-DDB-ROC1 ubiquitin ligase facilitates cellular response to DNA damage. *Mol Cell* 22: 383 – 394

Watanabe N, Arai H, Iwasaki J, Shiina M, Ogata K, Hunter T, Osada H (2005) Cyclin-dependent kinase (CDK) phosphorylation destabilizes somatic Wee1 via multiple pathways. *Proc Natl Acad Sci USA* 102: 11663 – 11668

Weissmann F, Petzold G, VanderLinden R, Huis In 't Veld PJ, Brown NG, Lampert F, Westermann S, Stark H, Schulman BA, Peters JM (2016) biGBac enables rapid gene assembly for the expression of large multisubunit protein complexes. *Proc Natl Acad Sci USA* 113: E2564 – E2569

Wynshaw-Boris A (2007) Lissencephaly and LIS1: insights into the molecular mechanisms of neuronal migration and development. *Clin Genet* 72: 296 – 304

Yin Y, Lin C, Kim ST, Roig I, Chen H, Liu L, Veith GM, Jin RU, Keeney S, Jasin M *et al* (2011) The E3 ubiquitin ligase Cullin 4A regulates meiotic progression in mouse spermatogenesis. *Dev Biol* 356: 51 – 62

Zou Y, Liu Q, Chen B, Zhang X, Guo C, Zhou H, Li J, Gao G, Guo Y, Yan C *et al* (2007) Mutation in CUL4B, which encodes a member of cullin-RING ubiquitin ligase complex, causes X-linked mental retardation. *Am J Hum Genet* 80: 561 – 566